Master's thesis

NTNU
Norwegian University of Science and Technology
Faculty of Natural Sciences
Department of Physics

Håvar Alexandersen

Resolved gravity waves in a high-resolution model

The interaction of gravity waves with planetary waves

Master's thesis in Applied Physics and Mathematics
Supervisor: Patrick J. Espy
Co-supervisor: Yvan J. Orsolini
June 2022

NTNU
Norwegian University of
Science and Technology

Håvar Alexandersen

Resolved gravity waves in a high-resolution model

The interaction of gravity waves with planetary waves

Master's thesis in Applied Physics and Mathematics
Supervisor: Patrick J. Espy
Co-supervisor: Yvan J. Orsolini
June 2022

Norwegian University of Science and Technology
Faculty of Natural Sciences
Department of Physics

NTNU
Norwegian University of
Science and Technology

Abstract

This thesis investigates the interaction between planetary and gravity waves in a high-resolution atmosphere model. Flow over mountainous terrain on Earth's surface can generate gravity waves. While propagating upward in the atmosphere, the amplitude grows exponentially. Potentially lead to wave breaking and dissipating energy locally, affecting the planetary waves. Planetary waves drive the general circulation in the mesosphere and lower thermosphere. It means small mountain ranges at the surface can impact the Earth's climate. The scale of gravity waves makes them demanding to resolve fully in climate models, but some high-resolution models partially capture the gravest part of the gravity wave spectrum. Simulation of July 1-10, by the high-resolution model WACCM5, is analyzed to detect and interpret the interaction between planetary and gravity waves.

By analyzing temperature fluctuations at approx. 68 km above remote mountain peaks in the south Indian Ocean, an anti-correlation is detected between the waves. These findings indicate that the breaking gravity waves attenuate the amplitude of the planetary waves, furthermore, the impact of these remote mountain peaks.

Sammendrag

Denne avhandlingen undersøker interaksjonen mellom planetære bølger og gravitasjonsbølger i en høyoppløst atmosfære modell. Luftstrømning over fjellterreng på jordens overflate kan skape gravitasjonsbølger. Amplituden vokser eksponentielt mens bølgen propagerer oppover i atmosfæren. Potensielt fører dette til at bølgen bryter og spre energien lokalt, som kan påvirke de planetære bølgene. Planetære bølger driver den generelle sirkulasjonen i mesosfæren og nedre del av termosfæren. Dermed kan små fjellkjeder på overflate kan påvirke jordas klima. Størrelsen på gravitasjonsbølger gjør de krevende å oppdage de fullstendig i klimamodeller, men noen høyoppløste modeller fanger delvis opp de groveste delene på gravitasjonsbølge-spekteret. Simulering av 1-10 juli i den høyoppløste modellen WACCM5 er brukt til å oppdage og tolke interaksjonen mellom bølgene.
Ved å analysere temperatursvingninger ved omtrent 68 km over avsidesliggende fjelltopper sør i Det indiske hav, ble en anti-korrelasjon funnet mellom bølgene. Funnene tyder på at amplituden til de planetære bølgene blir dempet av gravitasjonsbølger som bryter, og hvilken påvirkning disse avsidesliggende fjelltoppene har.

Preface

This master thesis isn't a story about one student working alone day and night. Some acknowledgments are deserved. To begin with, I would like to praise my two supervisors, Patrick J. Espy and Yvan Orsolini, for weekly meetings. These conversations gave me a lot; guidance, knowledge, confusion, and experience with the frustration of digital meetings. End of the day, without them, the tunnel would be long and dark, so thanks for pushing me in the right direction and using the amount of time to help me through. Their knowledge and expertise on the topic were crucial for this thesis. Thanks to Hanli Liu (National Center for Atmospheric Research, USA) for the amount of data made available, which allowed me to freely choose the direction of the thesis without any limitations from the data.

I want to thank the group of friends I have had the joy of spending five years together with, on and off campus. A special thanks to two of my classmates and friends, Maren Teien and Sveinung Seltveit. The way to long lunch breaks and good conversations were vital to getting through courses and on long days behind the keyboard. Finally, thanks to my girlfriend for pretending to find atmospheric waves fascinating, and forcing me to try to explain them in a way so she knew that I would be able to write it well. The help on figures, other advice, and support, in general, didn't go unnoticed.

Contents

Nomenclature

DALR Dry adiabatic lapse rate

GW Gravity wave

MLT Mesosphere and lower thermosphere

NCAR National Center for Atmospheric Research

NetCDF Network Common Data Format

PW Planetary wave

QGPV Quasi-geostrophic potential vorticity equation

WACCM The Whole Atmosphere Community Climate Model

WACCM-X The Whole Atmosphere Community Climate Model With Thermosphere and Ionosphere Extension

WACCM5 The Whole Atmosphere Community Climate Model version 5

List of figures

List of tables

1 Introduction

Everybody has a relation to the movement, or oscillation, of waves in the ocean. Small waves traveling towards a sunny beach or giant waves splashing over the deck of a container ship. The impact of these is clear to most of us. But what about the waves above us, in the atmosphere?

Atmospheric waves are of critical importance for the climate. The motions carry heat in a meridional flow, e.g. from the tropical regions to the poles. Consequently, reducing the extreme temperatures that would otherwise exist. The atmospheric waves, similar to the ocean waves, have a variety of wavelengths and times of existence. In general, small-scale waves transport momentum and energy upward, while the transportation from tropical regions to polar regions is mainly due to longer waves [15]. Gravity waves (GWs) fall in the category of small-scale waves in the atmosphere. They get generated in different ways, e.g. topographic launching or convective activity [12]. These triggers initiate adiabatic processes that lead to gravity and buoyancy forces trying to restore equilibrium. The air moves up and down until it settles at its initial position [7]. Contrary, planetary waves (PWs) fall in the other category and are very large-scale phenomenons. The spinning motion of the spherical planet, combined with pressure gradients displacing air, leads to the generation of planetary waves. The waves extend over thousands of kilometers and are of great significance for the meridional flow of heat and, by extension, the Earth's climate [15].

The broad scales of GWs and even broader scales of impact, from turbulence scale to planetary-scale, have made them difficult to include properly in a model [22]. For that reason, a high spatial resolution is necessary. Still, in circulation models, GWs are often parameterized due to the computational limitations [12]. In this thesis, a high-resolution simulation of July 1-10, provided by The Whole Atmosphere Community Climate Model version 5 (WACCM5) , is used. The simulation is of such a high resolution that it can resolve GWs partly.

The thesis investigates how the PWs and GWs interact and possibly affect each other. Given the scale difference, it is tempting to state that the impact is insignificant, but GWs can propagate upwards to the mesosphere and increase the amplitude exponentially. Hence, it can become unstable and break. Consequently, the wave dissipates energy and deposits momentum locally [34]. Lindzen [20] proposed

a simple theory about the effect of breaking GWs. They cause drag forces that decelerate the planetary waves to balance the momentum budget in the mesosphere. At the same altitude, Holton [17] suggested the breaking GWs causes the planetary wave to dissipate energy. A preliminary study characterized the wave scales present in the simulation [3]. The focus was on GWs in the mesosphere and lower thermosphere (MLT) . This study was a prelude to investigating the interactions with PWs. In this region of the atmosphere, GWs can reach high amplitudes. Hence, they can identify by temperature fluctuations [30].

Alexander et al. [2] findings indicate that the remote islands in the south Indian Ocean can be important in the interaction between waves in the atmosphere. A presentation, made by Alexander et al. [1], highlights the islands of Kerguelen, Heard, and McDonald as examples of this. These results and the findings in the preliminary study made this geographical location of interest to PW and GW interaction. To witness the impact of small, remote islands on PWs in the atmosphere, hence the general circulation.

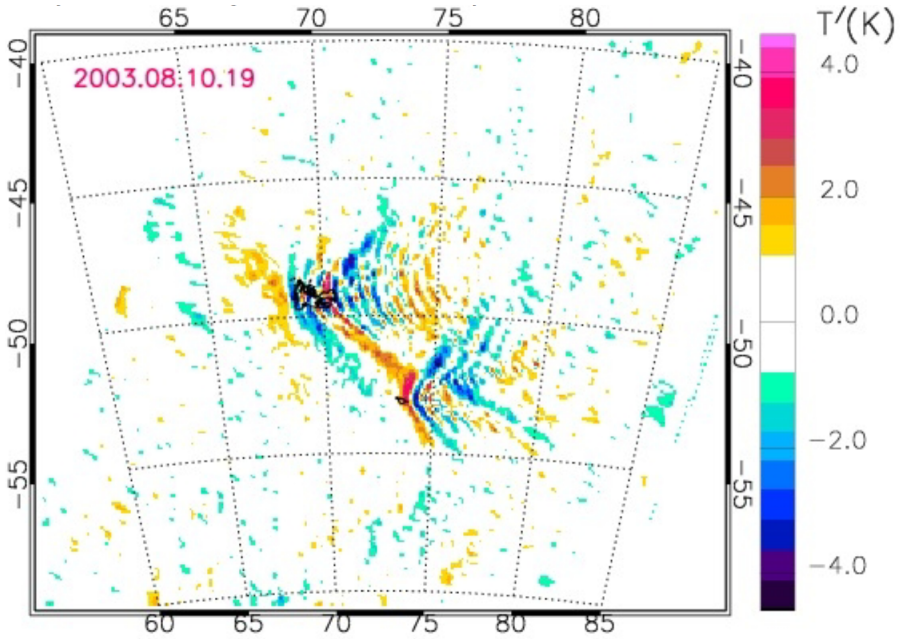

Figure 1.1: Temperature anomalies, $T'(K)$, derived from radiances measured in the AIRS on NASA's Aqua satellite. The upper islands are the Kerguelen Islands and the lower are Heard Island and McDonald Islands. Figure adapted from Alexander et al. [1].

2 Theory

For this thesis, it is of interest to know how the atmosphere is structured and defined. For studying the interaction between PWs and GWs, an introduction to the theory behind the waves is beneficial. This section includes a simplified physical explanation and a more mathematical description of the two different atmospheric waves.

2.1 Atmosphere - from us to outer space

Earth's atmosphere is divided into layers, defined by their different properties, i.e. the temperature gradient and pressure. Common for all is that density and pressure decrease with altitude, which culminates in the vacuum of outer space. For convenience, the layers can be grouped into the lower (troposphere), middle (stratosphere, mesosphere), and upper atmosphere (thermosphere, exosphere). The boundary altitudes between the layers vary with latitude and with the seasons, occurring higher in the summer and close to the Equator, and lower in the winter and near the poles [37]. With regards to GWs and PWs, the interest of this thesis is the MLT.

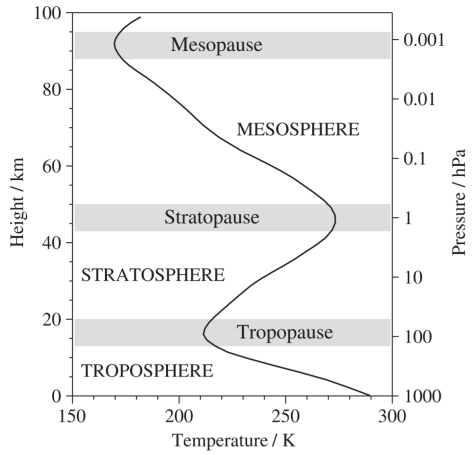

Figure 2.1: The layers of the atmosphere up to the mesopause. Also includes the temperature profile in connection to height and pressure. Figure by Andrews [6]

2.2 Gravity waves - Small waves growing exponentially

GW is a wave that is generated when the force of gravity or buoyancy tries to restore equilibrium. These waves may be generated in a fluid medium where the density is decreasing with height or at the interface between two media. A trigger mechanism displaces fluid parcels from equilibrium and the restoring forces will lead to an up and down movement of the fluid [4]. This thesis looks at internal GWs, which means GWs within a fluid medium. The medium in this case is the air in the atmosphere. GWs are most often generated in the troposphere. There may be different triggers, including airflow over mountains and convective activities.

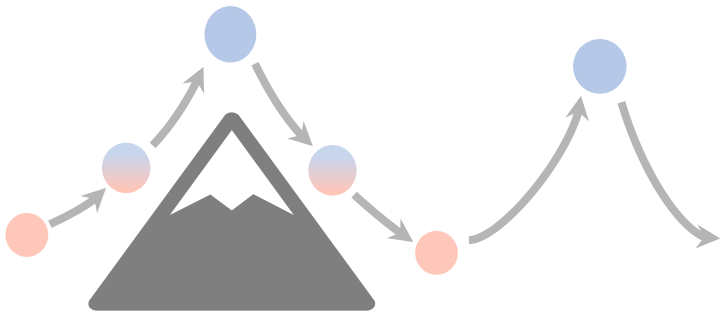

Figure 2.2: A parcel of air flowing over a mountain, generating GWs due to gravity and buoyancy forces trying to restore the parcel to equilibrium. This is often referred to as a lee wave. Figure made by the author.

2.2.1 A physical explanation of GWs

The explanation of the creation and propagation of PW presented below is inspired by a lecture given by Espy [9].

A good example of GW is when a rock is dropped in a pond, creating ripples on the surface boundary between air and water. The density difference between air and water is important in the generation

of the ripples/GWs. Density in the atmosphere decreases with increasing altitude. Looking at a small altitude difference, density can be thought to have a linear gradient. A parcel of dense air that is displaced from its initial position to a higher altitude will then be surrounded by less dense air. Gravity will act as a restoring force on, relatively, the heavier parcel, and pull it downward. The parcel can then overshoot its initial position and reach a lower altitude. Here, the surrounding air is denser and buoyancy will act on the lighter parcel and push it upward.

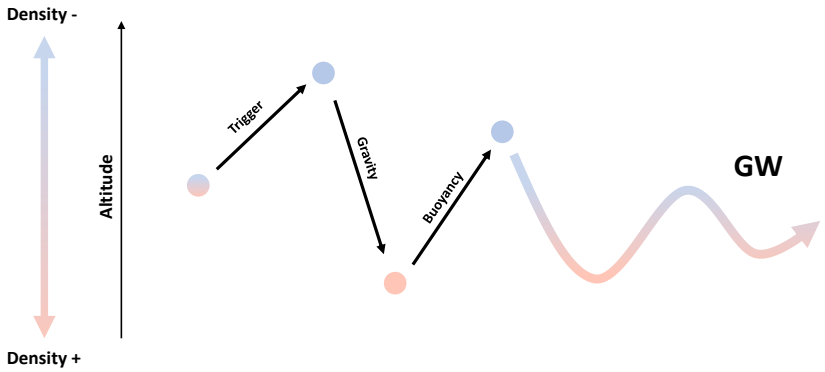

Figure 2.3: A trigger displaces a parcel of air to a higher altitude. Being heavier than the surrounding air, gravity pulls it downward before buoyancy pushes it upward again. This cycle continues, creating a GW. Figure made by the author.

This oscillating movement creates the GW. To be able to propagate away from the source of the initial displacement, a pressure disturbance is needed to create disturbances in adjacent columns. This way, the parcel can propagate and not just oscillate in the same place.

2.2.2 Mathematical description of GWs

This description and the following expressions are inspired by Andrews [4].

Common for all triggers, they make a parcel of air rise to an altitude of lower pressure. As the pressure decreases, the parcel expands and does thermodynamic work by pushing on the surroundings. Given that the thermal conductivity of air is low, and the size of the parcel is insignificant compared with the surrounding air, the heat transfer is negligible. Such a process, without any transfer of heat or mass, is called an adiabatic process. Therefore, the parcel does work but gains no heat. The first law of thermodynamics (1) states that the internal energy is then decreased, i.e. the temperature is reduced. The parcel undergoes adiabatic cooling.

$$dU = dQ - dW \tag{1}$$

$$dU = C_v n dT \tag{2}$$

The change in internal energy is dU, dQ denotes the changing energy of heat, dW is the thermodynamic work done by the system on the surroundings, C_v is the molar heat capacity, n denotes the mass (number of moles) and dT is the temperature change. The rewritten ideal gas law (3) defines the relationship between density ρ and temperature T.

$$\rho = \frac{pM}{RT} \tag{3}$$

Where p is pressure, M denotes the molar mass and R is the universal gas constant. A lower temperature leads to higher density, so the parcel of air becomes colder as it rises and expands. It becomes denser than the surrounding air at its new altitude, which makes the parcel start descending due to gravity. An important aspect of this process is the lapse rate Γ, the rate at which the ambient temperature decreases with altitude.

$$\Gamma(z) = -\frac{dT}{dz} \tag{4}$$

Where dz is the difference in altitude. The definition of an adiabatic process and the first law of thermodynamics (1) leads to:

$$c_p dT - \alpha dp = 0 \tag{5}$$

Where c_p is the specific heat capacity, α is the specific volume and dp is the change in pressure. Assuming an atmosphere in hydrostatic equilibrium, the net forces on any parcel of air must equal zero, the equation for hydrostatic balance can be utilized.

$$dp = -\rho g dz \tag{6}$$

The standard gravitational acceleration is denoted by g. Substituting the two equations (5) and (6) into the definition of lapse rate (4).

$$\Gamma = -\frac{dT}{dz} = \frac{g}{c_p} \tag{7}$$

Applying this to dry air leads to the dry adiabatic lapse rate (DALR) , and the value of approx. 9.8 °C/Km. This means that for every km the parcel ascends or descends, its temperature fall or rises 9.8 °C, respectively. Provided that the lapse rate of the surroundings is less than DALR, the process that generates GWs can occur.

The lapse rate of the atmosphere defines whether it is statically stable or statically unstable. This is crucial to generate the up and down motion. An atmosphere is stable when $\Gamma_{atmos} < \Gamma_{DALR}$, which prompts a displaced parcel to fall back towards its equilibrium, as described above. If the atmosphere were unstable, $\Gamma_{atmos} > \Gamma_{DALR}$, the parcel of air would at any time be less dense than the surroundings and therefore continue to rise. For does not experience any net force.

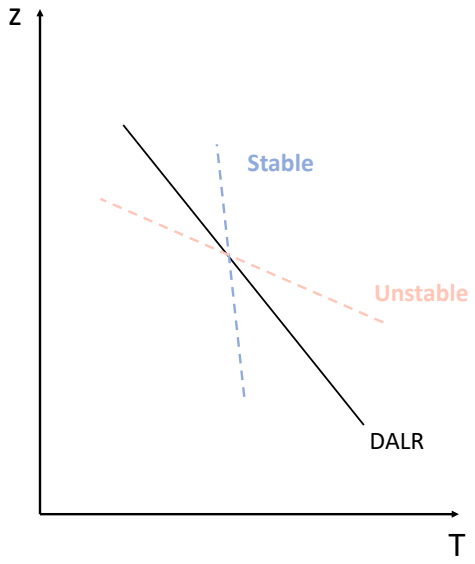

Figure 2.4: Lapse rate defines the change in temperature, T, with increasing altitude, z. Here, are DALR and examples of stable and unstable lapse rates. Figure made by the author, inspired by Andrews [4].

The upward buoyancy force acting on the parcel comes from Archimedes' principle.

$$F = gV_{pl}(\rho_{sur} - \rho_{pl}) \tag{8}$$

V_{pl} and ρ_{pl} denote the volume and density of the parcel, respectively. The density of the displaced surrounding air is ρ_{sur}. Newton's second law states that this force equals the mass of the parcel times its acceleration:

$$F = V_{pl}\rho_{pl}\frac{d^2(z)}{dt^2} \tag{9}$$

Combining these equations to get an expression for the acceleration of the parcel.

$$\begin{aligned}\frac{d^2(z)}{dt^2} &= g\left(\frac{\rho_{sur}}{\rho_{pl}} - 1\right) = g\left(\frac{T_{sur}}{T_{pl}} - 1\right) \\ &= g\left(\frac{T - \Gamma_{pl}dz}{T - \Gamma_{sur}dz} - 1\right) = g\left(\frac{\Gamma_{sur} - \Gamma_{pl}}{T - \Gamma_{sur}dz}\right)dz \\ &= -\frac{g}{T}(\Gamma_{pl} - \Gamma_{sur})dz\end{aligned} \tag{10}$$

In the derivation, equations (3) and (4) were utilized. Equation (10) can be rewritten to define the buoyancy frequency or the Brunt-Vãisãlã frequency, N.

$$\frac{d^2(z)}{dt^2} + N^2(dz) = 0 \tag{11}$$

Leading to the expression for the buoyancy frequency:

$$N^2 = \frac{g}{T}(\Gamma_{pl} - \Gamma_{sur}) = \frac{g}{T}\left(\frac{dT}{dz} + \frac{g}{c_p}\right) \tag{12}$$

The Brunt-Vãisãlã frequency is the frequency that a parcel freely oscillates up and down. In the context of GWs, the Brunt-Vãisãlã frequency can be utilized to relate the horizontal and vertical wavelength, and GW oscillation is always less than N.

2.2.3 How GWs propagate energy

All of the above theory is important and explains how a GW can occur, but a key aspect of these waves is momentum and energy transportation. Waves that are generated in the troposphere can propagate vertically up into the stratosphere and mesosphere. A simplified explanation and visualization of how this happens are given by Hocking [16].

Looking at a corrugated sheet moving through the still air and how the sheet affects the air parcels. The surface of the corrugations will appear to move upward (or downward) and forward with increasing time as shown in figure 2.5. This means the parcels in the respective regions will achieve a velocity component both upward (downward) and forward. The parcels being displaced up and forward undergoes adiabatic cooling. In the other region, the parcels will undergo the opposite, adiabatic heating.

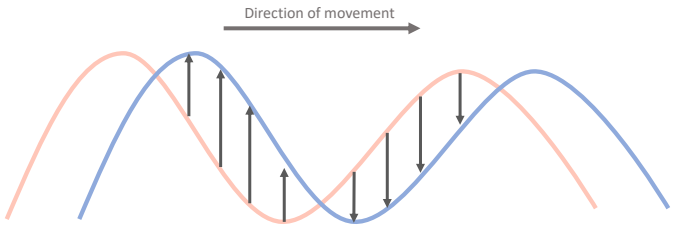

Figure 2.5: The red line represents the corrugated sheet at one instant, and the blue line is the same sheet a short time later. The regions with arrows appear to displace upward and downward, as well as forward with respect to the movement. Figure made by the author, inspired by Hocking [16].

In figure 2.6, the air parcels at point A are being displaced according to figure 2.5, this means the air at A will be displaced upward and toward the right. The displacement creates a positive pressure perturbation relative to the air columns' equilibrium. However, each parcel of air between A and the peak (to its left) is displaced to pressures lower than its equilibrium position. Consequently, the rising air expands and cools from its equilibrium value. When the air reaches the peak between A and B' this expansive-cooling will be maximum. Tipping over the peak and falling down towards B' causes the air to begin compressing and heating from the value it had at the peak. The air parcel will reach its equilibrium value at the hypothetical line B'-A-B, before it continues to compress and heat to a maximum pressure and temperature at the trough.

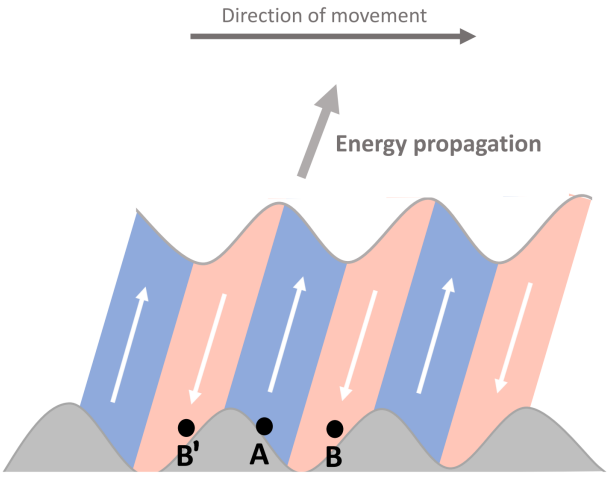

Figure 2.6: The bottom corrugated sheet in motion, surrounded by still air, visualizes the energy propagation. The red and blue regions represent, respectively, regions of upwards and downwards displacement. The white arrows are the direction of the displacement. Air parcels in the blue regions (represented by A) undergo adiabatic cooling, while parcels in the red regions (represented by B' and B) undergo adiabatic heating. This creates a new sheet that continues the same process upwards. Figure made by the author, inspired by Hocking [16].

A new corrugated sheet will be generated by the parcels' displacement. Hence, the first sheet transfers energy into the new sheet/wave, and this process will continue, leading the energy transportation to propagate throughout the atmosphere. As displayed in figure 2.1, further up in the atmosphere the pressure decreases, meaning that the surrounding air gets less dense. To obey the conservation of energy, the amplitude of the waves (corrugations in this explanation) increases exponentially with altitude to compensate for the decreasing surrounding density. If the amplitude reaches its breaking point, the wave becomes non-linear and unstable. It overturns and deposits its energy and momentum locally, just like a wave in the ocean produces whitecaps and "hits itself".

The horizontal and vertical wavelength is defined, respectively, as the horizontal and vertical distance between two identical wavefronts. By using figure 2.7, this means, for the horizontal (for the vertical), the distance parallel (perpendicular) with the movement of the sheet from a point on a blue line to another blue line. The ratio between the wavelengths can describe the orientation and propagation direction of the particular GW. As seen in figure 2.7, the orientation of the waves is important for the direction of the energy transport. Section 2.2.4 determines this relation mathematically.

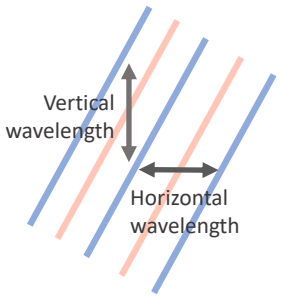

Figure 2.7: Visualization of the horizontal and vertical wavelength. The lines can be thought of as the intersection between regions in figure 2.6. Figure made by the author, inspired by Hocking [16].

2.2.4 Modeling GWs mathematically

To develop a model for GW, a practical description from Andrews [5] is to look at the plane-wave solutions of the linear Boussinesq equations. To obtain these, the Boussinesq approximation is implemented. The density variations are neglected, except for those that are coupled with gravity. Some other approximations can be used for solving this, given that GW is relatively small atmospheric waves. The terms introduced by the Coriolis force can be neglected, as well as assuming that buoyancy frequency (N_B) is independent of z, the altitude. From figure 2.1 and equation (12), this is a plausible assumption for the two lowest layers, where the lapse rate is as good as constant.

The resulting Boussinesq equations is:

$$\frac{du}{dt} + \frac{1}{\rho_0}\frac{dp'}{dx} = 0, \tag{13a}$$

$$\frac{dv}{dt} + \frac{1}{\rho_0}\frac{dp'}{dy} = 0, \tag{13b}$$

$$\frac{du}{dx} + \frac{du}{dy} + \frac{du}{dz} = 0, \tag{13c}$$

$$-\frac{g}{\rho_0}\frac{d\rho'}{dt} + N_B^2 w = 0, \tag{13d}$$

$$\frac{dp'}{dz} + gp' = 0 \tag{13e}$$

Here, u, v and w is velocities in the different directions, ρ' is the density deviation, ρ_0 is constant value for the density and p' is then the pressure deviation. The plane waves are in the form:

$$[u, v, w, p', \rho'] = Re[\hat{u}, \hat{v}, \hat{w}, \hat{p}, \hat{\rho}]e^{i(kx+mz-\omega t)} \tag{14}$$

The plane wave is traveling in the x-direction and oscillating in the z-direction, independent of y, with angular frequency ω. The $\hat{u}$ etc. are complex amplitudes, while k and m are x- and z-component of the wave-vector, respectively.

$$-i\omega\hat{u} + \frac{ik\hat{p}}{\rho_0} = 0, \tag{15a}$$

$$-i\omega\hat{v} = 0, \tag{15b}$$

$$ik\hat{u} + im\hat{w} = 0, \tag{15c}$$

$$\frac{i\omega g\hat{\rho}}{\rho_0} + N_B^2\hat{w} = 0, \tag{15d}$$

$$im\hat{p} + g\hat{\rho} = 0 \tag{15e}$$

Inserting equation (14) and choosing to keep $\hat{p}$, as well as arbitrarily choosing it to be real, the resulting definitions can be shown:

$$p' = \hat{p}cos(kx + mz - \omega t), \tag{16a}$$

$$u = \frac{k\hat{p}}{\rho_0 \omega} cos(kx + mz - \omega t), \tag{16b}$$

$$v = 0, \tag{16c}$$

$$w = \frac{k^2 \hat{p}}{\rho_0 \omega m} cos(kx + mz - \omega t), \tag{16d}$$

$$\rho' = \frac{m\hat{p}}{g} sin(kx + mz - \omega t) \tag{16e}$$

The non-trivial solution to equations (15) leads to the dispersion relation for internal GWs:

$$\omega^2 = \frac{N_B^2 k^2}{m^2} \tag{17}$$

To be able to understand the physical aspect of the two different solutions for ω in the dispersion relation, it is helpful to introduce the group velocity:

$$\vec{c}_g = \left(\frac{\partial \omega}{\partial k}, 0, \frac{\partial \omega}{\partial m}\right) = \left(\pm \frac{N_B}{m}, 0, \mp \frac{N_B k}{m^2}\right) \tag{18}$$

A reasonable convention is that wave number k is a positive value. For GW generated near the ground, as for most waves, the group velocity will be the velocity at which the energy propagates. As described in relation to figure 2.6, this is in a positive z-direction, leading to $c_g^{(z)} > 0$. Consequently, the solution for the dispersion relation (17) is the negative:

$$\omega = -\frac{N_B k}{m} \tag{19}$$

Figure 2.8 illustrates the relations between the different variables. A key resulting feature is than if $\omega > 0$, then $m < 0$. The wave will move in the direction of the wave-vector $(k, 0, m)$, e.i. positive x-direction and negative z-direction, as shown in figure 2.8. The GW has a direction downward, while the group velocity and thus the energy propagation is upwards.

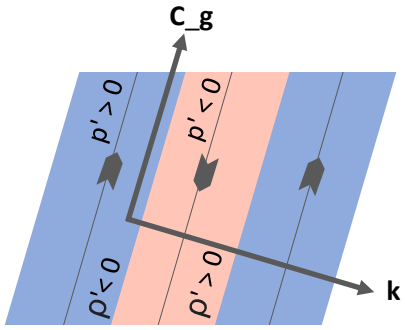

Figure 2.8: A vertical cross-section through a plane internal GW with $k > 0$, $\omega > 0$ and $m < 0$ so that $c_g^{(z)} > 0$. The long black arrowheads represent the velocity vectors in the regions. The greatest positive and negative of the pressure and density disturbance are marked. The blue regions have upward motion, while the red has downward. The large arrows represent the direction of the group velocity (c_g) and the direction of the wave-vector k. The different regions will move perpendicular to each other but in the direction of k. Figure made by the author, inspired by Andrews [5].

2.3 Planetary Waves - Large waves transporting heat

The generation of the movement of a PW is a result of the conservation of potential vorticity and pressure gradients. The spherical geometry of the Earth is crucial in this process. The wavelength of a PW can be on a global scale and it only has a westward movement [7]. Given the scale of the waves, they are of great significance for the heat flow between the tropic and the polar regions. A wavenumber 1 PW is defined as a wave with one trough and one crest over the full 360 degrees of longitude. The same analogy applies for wavenumber 2,3, etc.

2.3.1 A physical explanation of PWs

The explanation of the creation and propagation of PW presented below is inspired by a lecture given by Espy [10].

A non-rotating observer (black person in figure 2.9) looks down from the sky on a barrel of water with a paddle at the North Pole. From this frame of reference, the paddle has a spin of one rotation over 24 hours. Likewise, placing a barrel at the Equator, the spin of the paddle would be zero. Changing the frame of reference to a rotating frame, an observer (grey person in figure 2.9) standing next to the barrels will detect no spin at the North Pole or the Equator.

Now, the barrel at the pole is instantaneously transported right next to the one at the Equator. Both barrels will stand still, as expected, but the water and paddle from the pole will have the same one rotation a day spin. This can be observed independent of the frame of reference. The relative vorticity of the pole paddle is different than the planetary vorticity at this location, making it spin anti-clockwise relatively. Conversely, the vorticity of the equatorial paddle would differ from the planetary vorticity at the pole, giving the latter a clockwise spin relative to the planet.

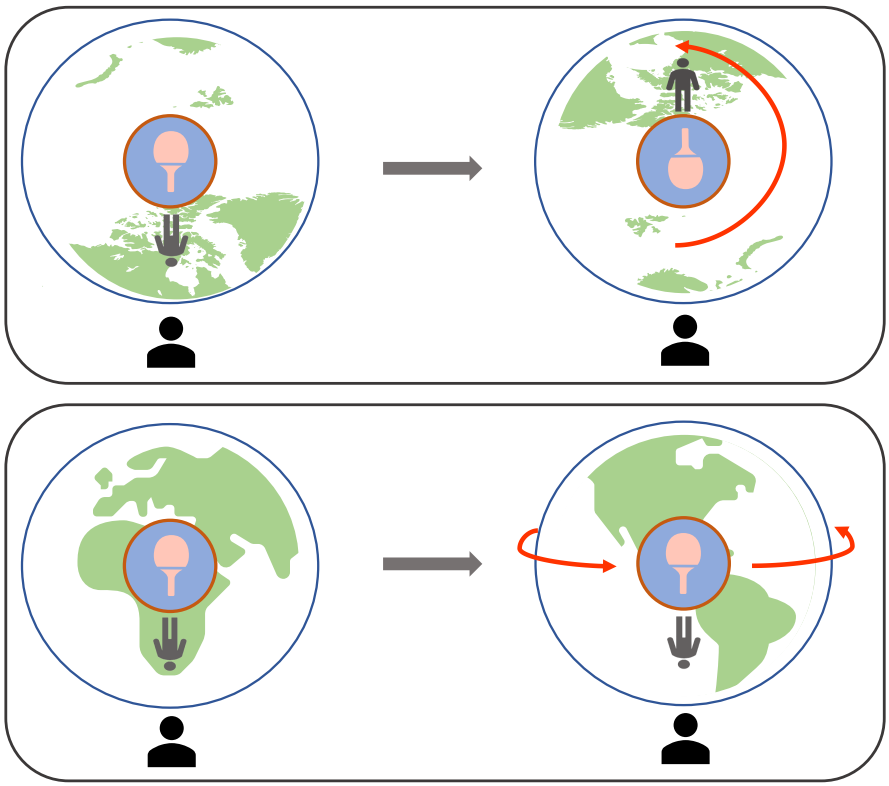

Figure 2.9: The black person represents a non-rotating observer and the grey represents a rotating observer. Displays how the spin of an object (here: paddle) is relative to the frame of reference and placement on Earth. The red arrows represent the rotation of the planet. (a) Barrel of water with a paddle placed at the North Pole. (b) Barrel of water with a paddle placed at the Equator. Figure made by the author.

This example is an extreme case, nevertheless, a difference in the vorticity will occur for any displacement in latitude. If now the barrel of water would be a parcel of air, the disturbance by the spin relative to its surroundings would lead to a movement to the west. Any displacement to lower latitudes (A in figure 2.10) causes an anti-clockwise spin relative to the surrounding air. Thereby dragging the air to the west towards lower latitudes, and conversely air to the east to higher latitudes. The same idea can be applied to displacements of parcels towards higher latitudes (B in figure 2.10). Here, the parcels obtain a spin clockwise spin relative to the surrounding air and drag air to the west towards higher latitudes and to the east to lower latitudes. The result is a westward propagation and is depicted in figure 2.10.

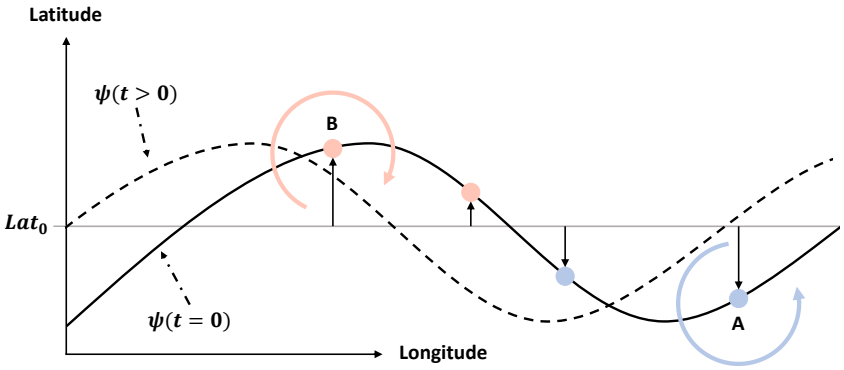

Figure 2.10: The red dots are displaced upwards from their initial position (Lat_0), leading to a clockwise spin. While the blue dots are displaced downwards, leading to an anti-clockwise spin. Conversely, make the wave propagate from its original position (t=0) towards the west (t > 0). Figure made by the author.

2.3.2 Mathematical description of PWs

This description and the following expressions are inspired by Andrews [5] and Salby [32].

As mentioned, vorticity is of great importance when describing PWs. The absolute vorticity can be defined as followed:

$$f + \xi \tag{20}$$

$$\xi = \frac{\partial v}{\partial x} - \frac{\partial u}{\partial y} \tag{21}$$

$$f = 2\Omega \, sin \, \phi \tag{22}$$

From equation (20), absolute vorticity is the sum of relative vorticity (21) and planetary vorticity (22). The planetary vorticity, f, is often introduced as the Coriolis parameter, with Ω as angular velocity and ϕ as latitude. By considering a non-divergent barotropic fluid, the absolute vorticity is constant.

As a parcel of air is displaced towards the north in an eastward wind, there is a change in the components of the sum. To conserve absolute vorticity, ξ decreases as the latitude increases, and consequently f. The decreased ξ leads to a clockwise spin, displacing the parcel back towards the south and its initial latitude ϕ_0. Upon overshooting ϕ_0, the opposite happens, f decreases, and ξ increases, leading to an anti-clockwise spin. As this continues, the parcel of air will cycle back and forth about its initial latitude.

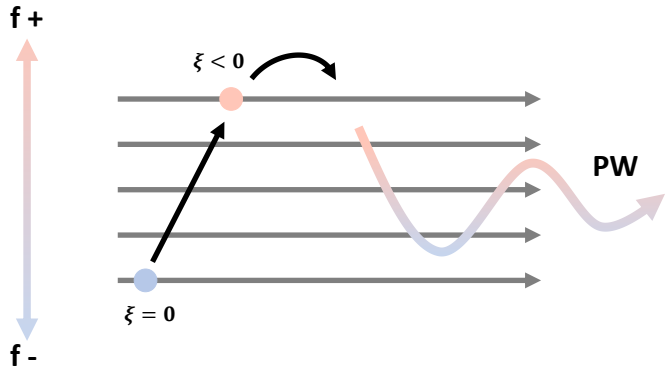

Figure 2.11: The parcel is displaced northward in an eastward current. To obtain constant absolute velocity, ξ decreases as a result of an increase in f. This cycle continues, creating a PW. Figure made by the author.

To describe PW further, the beta approx. for the variation of the Coriolis parameter is used.

$$f = f_0 + \beta y \tag{23}$$

Where f_0 is a constant value of f at ϕ_0 and β is the derivative of f with respect to y, allowing f to vary linearly with the northward distance y. By definition, $\beta > 0$, increasing from the south to the north. Introducing the quasi-geostrophic potential vorticity equation (QGPV) , which is derived in Andrews [5].

$$\frac{D}{Dt}(\xi + \beta y) = 0 \tag{24}$$

The total flow is given by:

$$\psi = -Uy + \psi'(x, y, t) \tag{25}$$

U is a constant uniform background zonal flow $(U, 0, 0)$ and ψ' corresponds to a perturbation stream function. Writing out and linearising QGPV (24) gives:

$$\frac{\partial}{\partial t}\nabla^2\psi' + U\frac{\partial \nabla^2\psi'}{\partial x} + \beta\frac{\partial \psi'}{\partial x} = 0 \tag{26}$$

Looking for plane-wave solutions to this equation of the form:

$$\psi' = Re\ \tilde{\psi} e^{i(kx+ly-\omega t)} \tag{27}$$

Where $\tilde{\psi}$ is a complex amplitude. Substituting this waveform into equation (26) gives the dispersion relation for PWs (for $\tilde{\psi} \neq 0$ and $m = 0$).

$$\omega = kU - \frac{\beta k}{k^2 + l^2} \tag{28}$$

From the dispersion relation (28), the phase velocity (c) and group velocity (c_g) can be defined quite simply.

$$c = \frac{\omega}{k} = U - \frac{\beta}{k^2 + l^2} \tag{29}$$

$$c_g = \frac{\partial \omega}{\partial l} = U + \frac{\beta(k^2 - l^2)}{(k^2 + l^2)^2} \tag{30}$$

Since β is defined as a positive value, the phase velocity will always be less than the background flow. Meaning that PWs always propagate westward relative to the background flow.

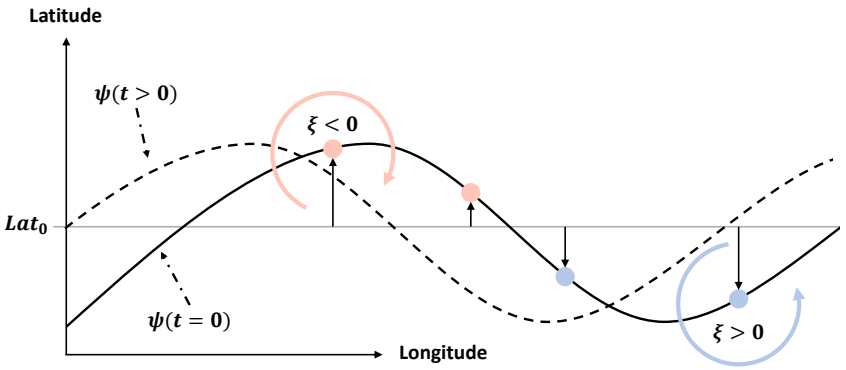

Figure 2.12: The red dots are displaced upwards from their initial position ($\xi = 0$), leading to negative planetary vorticity. While the blue dots are displaced downwards, leading to positive planetary vorticity. Conversely, make the wave propagate from its original position (t=0) towards the west (t > 0). Figure made by the author.

3 Method

In this thesis, the data obtained from an atmospheric climate model were analyzed and examined. The aim was to visualize and study the interaction between PWs and GWs, focusing on a specific wave packet of GWs at a given altitude. The data examined is from July 3 to July 9. This section gives a description of the model creating the data and the approach to examining the interaction.

3.1 The model of the atmosphere: WACCM5

The data used are from a high-resolution version of WACCM . The high resolution enables the model to resolve GW partly. The model is one of the atmosphere components of the NCAR Community Earth System Model version 1. The simulation is over a short period, from July 1-10, due to the high-resolution Liu [23]. It is started from a climatological state, meaning that the result does not represent the actual atmosphere of this period, but a model realization of the atmosphere. The version used in this study is the spectral element of WACCM5 and is described comprehensively by Liu et al. [22].

The main feature related to this paper is the fact that the simulation is high-spatial resolution. The grid is based on a cubed sphere, as depicted in figure 3.1. The spatial resolution is about 0.23 degrees latitude and 0.31 degrees longitude, meaning the simulation provides data for every 0.23 degrees and 0.31 degrees respectively. The vertical domain extends to 5.96×10^{-6} hPa, approx. 145 km above Earth's surface. This domain is divided into 209 levels, with increasingly spacing upward in the atmosphere. The top layers (above 10^{-4} hPa) are sponge layers with increasing damping, as the GWs amplitude grows exponentially. The GW parameterization employed in the model has been adjusted for the high-resolution configuration to obtain a realistic background wind and temperature structure. Historically, the parameters are chosen to be physically reasonable and give results consistent with observations [13]. Liu [23] goes further into detail on the adjusting of parameters in this model.

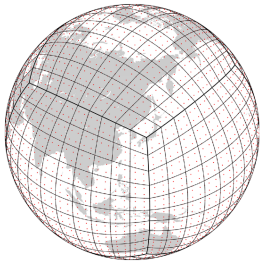

Figure 3.1: An example of a cubed sphere grid, as used in WACCM5. The resolution is about 25 km in the simulation for July 1-10, which is used in this paper. Figure by Kim et al. [18].

3.1.1 The data from the simulation

The data for each day in the simulation was stored in the file format NetCDF. NetCDF software is developed by UCAR/Unidata, and the format is regularly used for scientific data, given the conventional structure and accessibility [36]. Both Matlab and Python were used to work with the data. In Python, it was simple to get an overview of the structure of the file and its content, as well as produce contour plots. While Matlab was preferable when it came to more complex analysis. As illustrated in figure 3.2, the file from each of the days had four coordinates (including time) that the variables could be dependent on. The coordinates and variables from the simulation used in this report are presented in table 1, and table 2 in the appendix presents all available coordinates and variables.

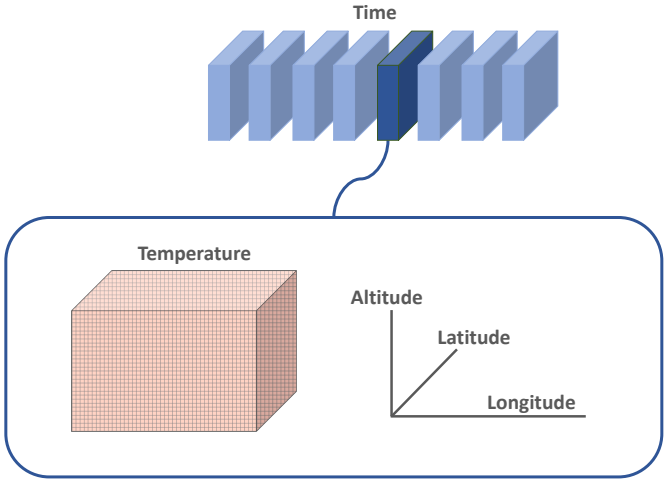

Figure 3.2: Visualization of the NetCDF format structure, which contained the data from WACCM5. Shows the structure of one day of data. Figure made by the author.

Table 1: The coordinates (coord) and variables (var) used for each day, given by the data set from the WACCM5 simulation. Given that T was dependent on all four coordinates, it had over 4.4e9 values for one day.

Name	Type	Long name	Dependence	Dimension	Units
lev	coord	Hybrid level at midpoints	-	209	hPa
time	coord	Time	-	24	hours
lat	coord	Latitude	-	768	degrees north
lon	coord	Longitude	-	1152	degrees east
T	var	Temperature	time,lev,lat,lon	-	K

3.2 Approach to detect interactions between PW and GW

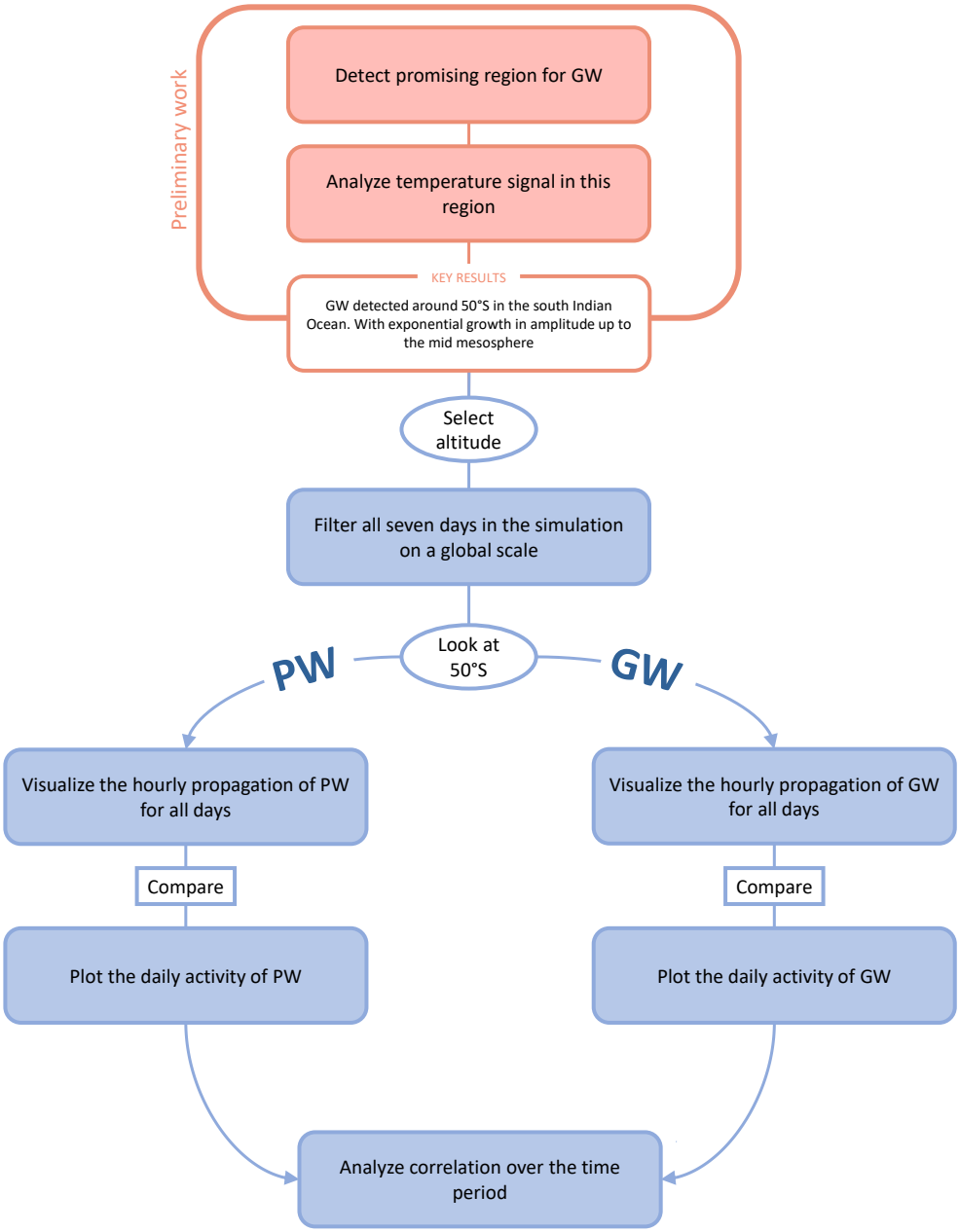

Figure 3.3: Visualization of the tentative plan for inspecting interactions between PW and GW in the data from WACCM5. The blue ovals are based on preliminary results. Figure made by the author.

4

Results

All the results gathered from the data are provided from the simulation of July 1-10 [25]. The specific dates for the available files were July 3 to July 9. The results are based on the preliminary work done in the project report [3], this section includes the most significant findings. The analysis in this thesis is on a fixed latitude, 50°S. The reason behind this choice is the results found in the mentioned prelude. The most relevant findings from that report are in this section. The section includes a brief description of how the different results are found.

Through using the Xarray package in Python, the NetCDF files for July 3 to July 9 were read. The chosen variable was temperature, and the zonal mean was subtracted. By taking the zonal mean out, the general temperature difference between the northern and southern hemispheres was removed. This was done to better visualize local structures in the contour plots. Temperatures at each of the 209 altitude levels were plotted. At level 92 some significant structures could be detected in the southern hemisphere. This corresponds with 0.052 hPa, approx. 70 km [29], and was selected to analyze further. Large structures (PW) of the global plot were filtered out by using a median filter [27]. Hence, the remaining were relatively small structures (including GW). An area a bit east on the latitude 50°S was recognized as a region of interest.

The contour plot in figure 4.1 shows the filtered temperature on a global scale. There is a good amount of structures, and the temperature scale is altered to increase the contrasts in the plot. The southern region from 30°S to 70°S, marked by dotted red lines, contains a significant amount of structures. Figure 4.3 depicts this region. There are two notable domains of this region that have defined small structures. The domains are from -100°E to 0°E and 50°E to 150°E. The latter domain displays less structure but is marked by red lines as the region of interest in figure 4.2. The reason for this is that from -100°E to 0°E the peninsulas called the Southern Cone and the Antarctic Peninsula will be the dominant sources of the GWs [39], and this report wanted to explore the smaller and more remote sources.

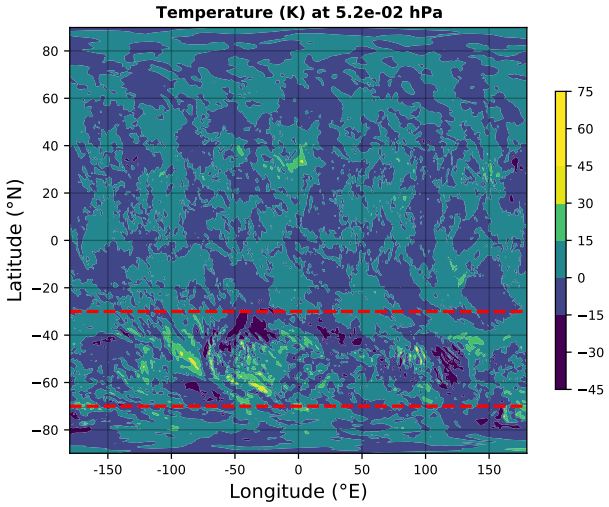

Figure 4.1: Temperature fluctuations in the atmosphere of Earth. By filtering and contrast stretching, the small structures are highlighted. In the red region, there is predominant when accounting for small structures. Reprinted from Alexandersen [3], and the data used is from July 4.

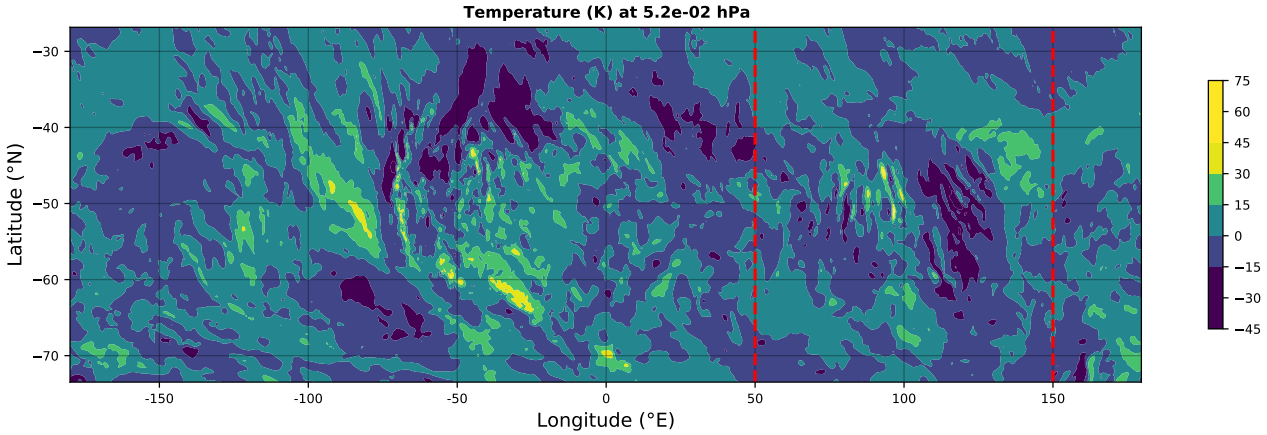

Figure 4.2: The band in the southern hemisphere has a significant amount of small structures. The marked area is the region of interest. Reprinted from Alexandersen [3], the data used is from July 4.

Figure 4.3 shows a region of interest. There are about 6 hot spots in the region from 70°E to 100°E around the same latitude, −50°N. Relative to the scale of this domain, there is some larger structure present.

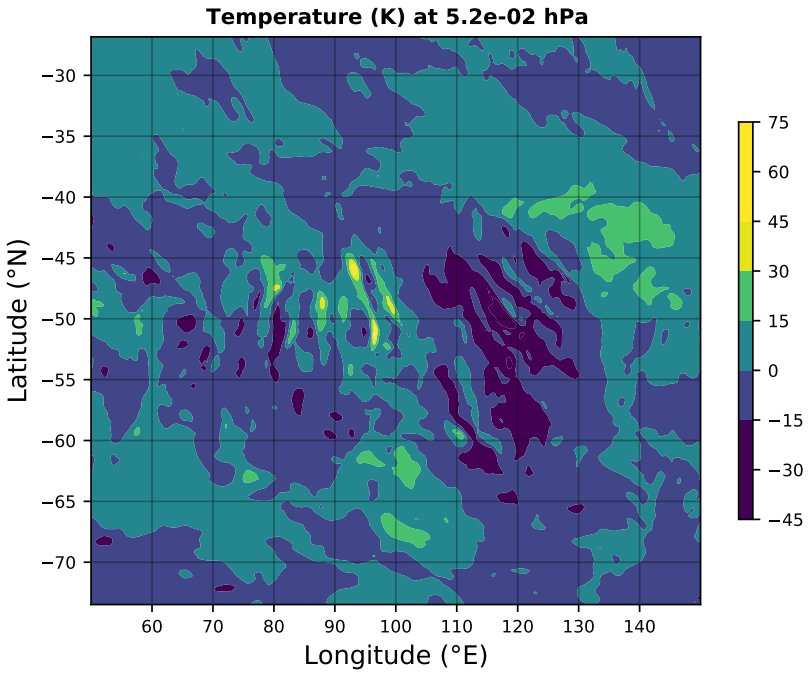

Figure 4.3: Region of interest. Central in the region is a few significant hot spots, around -50°N. Reprinted from Alexandersen [3], the data used is from July 4.

To be able to obtain these hot spots as a signal, the smaller domain was sliced through the latitude 50°S. The dominant wavelength of these waves were identified using a Lomb-Scargle algorithm, and its amplitude vs. altitude was determined by fitting sine waves at each altitude. The Lomb-Scargle periodogram was found by using a built-in function in Matlab with this signal as the input [26]. Through CFTool [8] in Matlab, the sinusoidal could be fitted. CFTool lets the creation of a fit be transformed into Matlab code. This way the code was used for all the 209 levels, allowing the amplitude and phase of the sinusoidal to vary. Consequently, the GW propagation could be tracked downward, as well as upward.

In figure 4.4 the amplitude of the GW is plotted in term of temperature, as a function of altitude. Both the vertical and horizontal axis is on a logarithmic scale. A dotted trendline is plotted and displays an exponential growth of the amplitude. Above this trendline, the amplitude becomes more chaotic. The altitude where the pressure is 6.4e-2 hPa is marked with a horizontal red line. Here, the amplitude of

the GW is seemingly at its largest.

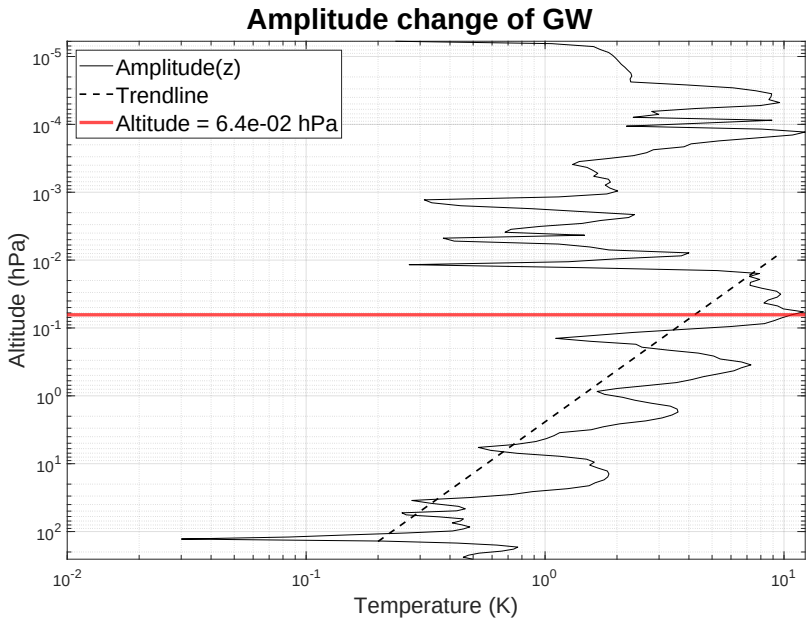

Figure 4.4: The chosen altitude of 6.2e-2 hPa is marked on a plot of the amplitude change of the GW. The trendline displays the trend of exponential growth of the amplitude. Adapted from Alexandersen [3], the data used is from July 4.

From figure 4.4 of the vertical propagation, the altitude of 6.4e-2 hPa, approx. 68 km [29], were chosen to be most suited to see the interaction of the GW with the temperature and wind perturbations caused by the PW. The upcoming analysis and results are at this altitude.

The same procedure as mentioned earlier, with subtracting zonal mean temperature and median filtering, was applied to all seven days. The PWs were stored as well as subtracted to obtain the small structures, including the GW. With a focus on the latitude 50°S, the hourly longitudinal propagation of both waves were visualized for each day. PW for all longitudes and GW on the smaller region of interest.

The longitudinal propagation of a PW is depicted in figure 4.5. Each of the seven days in July has a contour plot of the temperature change over 24 hours. The plots are over 360° of longitude. All days have a higher temperature on the left side, while the right side is significantly colder. In general, the seven days have similar features, but the tendency is that the pattern moves towards right the following day. Over the period, the wave patterns movement is about 60° in longitude. Figure 4.6 depicts the longitudinal propagation of a GW. Similarly to figure 4.5, each of the seven days has a contour plot over the 24 hours. The range of longitude is from 70°E to 110°E. The different plots display quite a unique pattern, but they all have a common two-colored striped background pattern. In some, there are significantly higher fluctuations in temperature present. July 4 and July 7 stand out in this respect. In general, all have wave patterns oriented toward the right, to a bit different degree.

Figures 4.5 and 4.6 are presented sideways on the next pages to display the plots with the most accuracy.

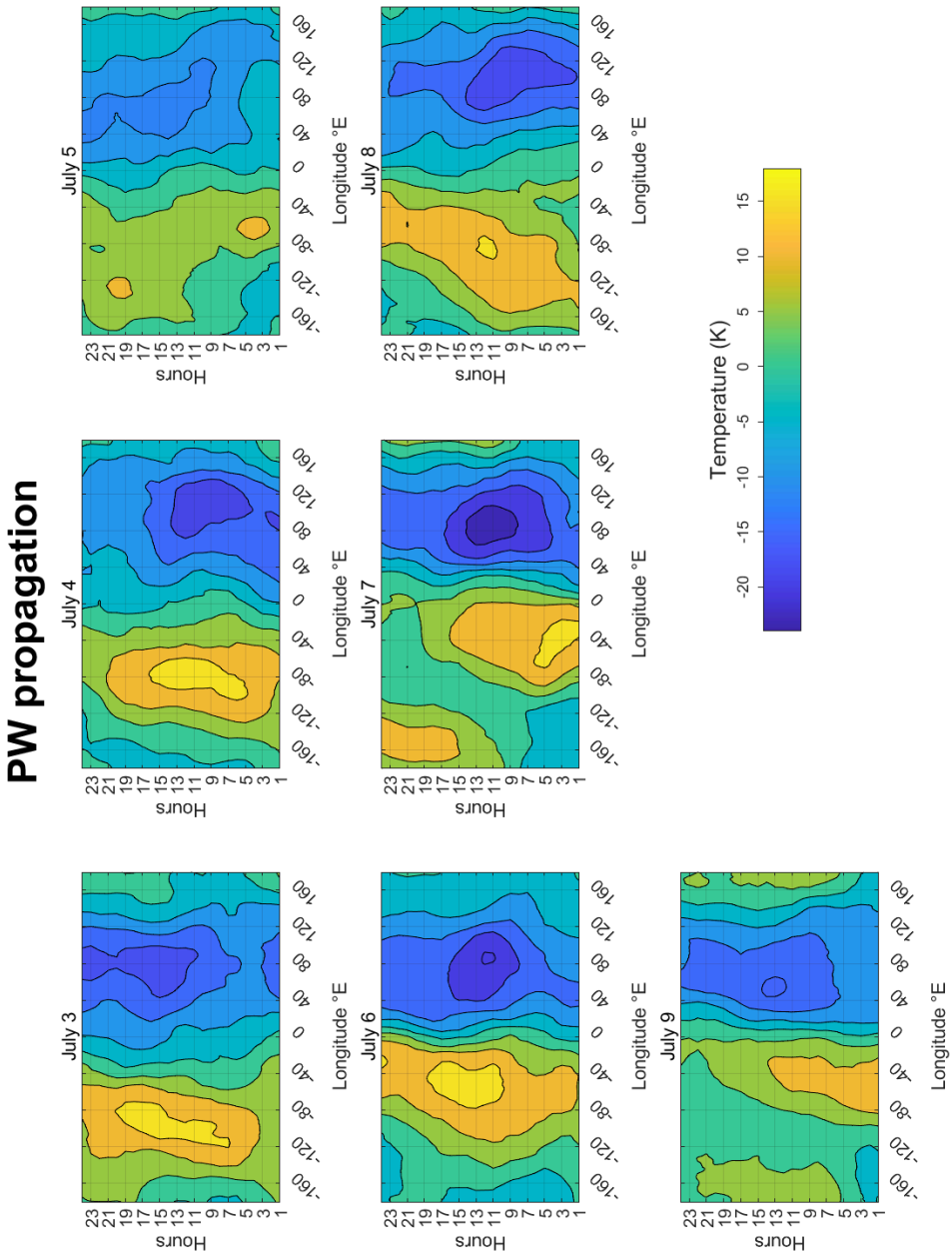

Figure 4.5: The PW in temperature during the seven different days in July, at 50°S. Shows the longitudinal propagation at this latitude.

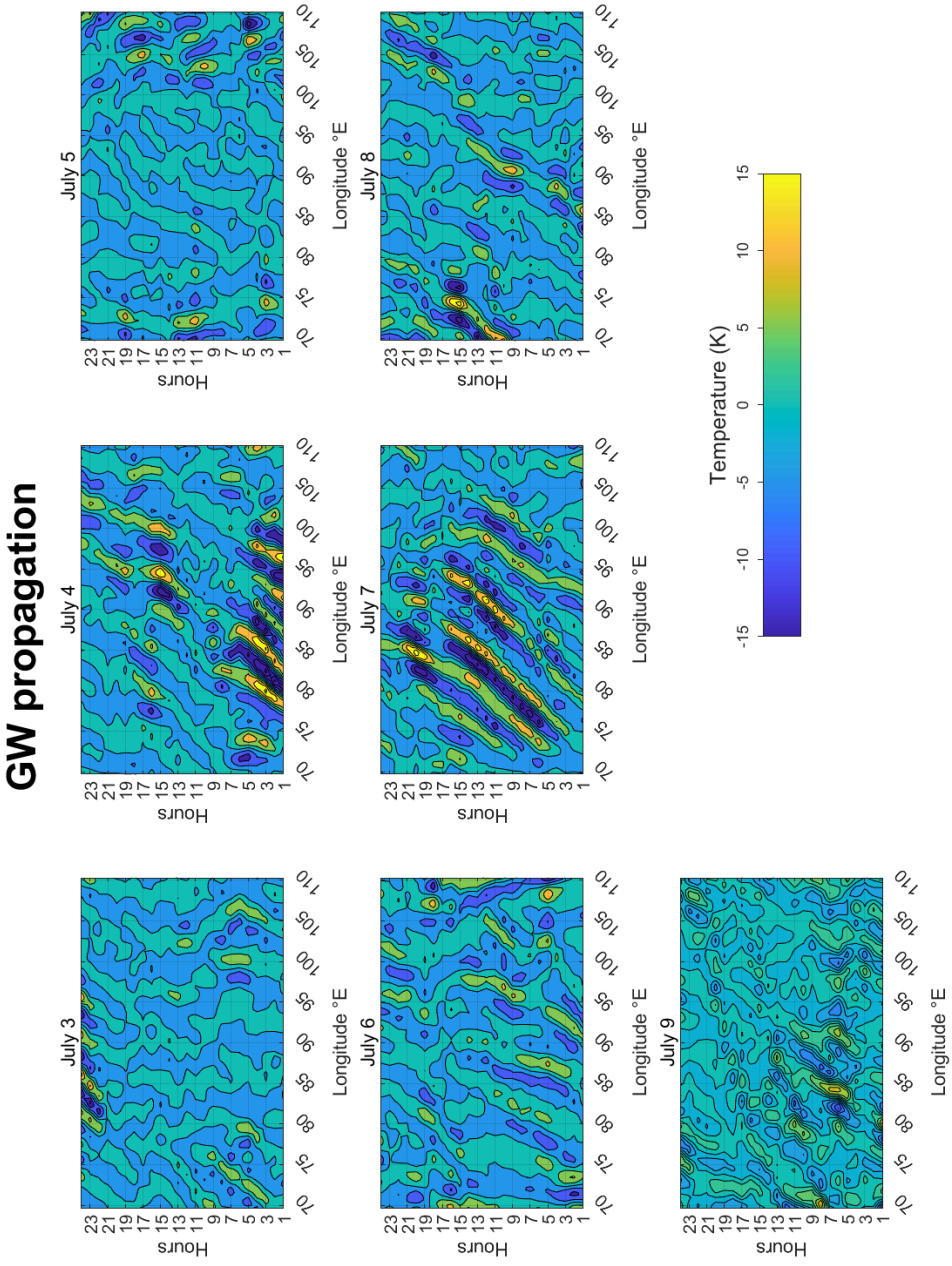

Figure 4.6: The GW in temperature during the seven different days in July, at 50°S. The contour plots display a specific range of longitudes.

To isolate the desired GW, filterDesigner [11] in Matlab was used to design a band-pass filter. The filter was designed for hour 2 of July 4 and applied on all hours of all seven days.

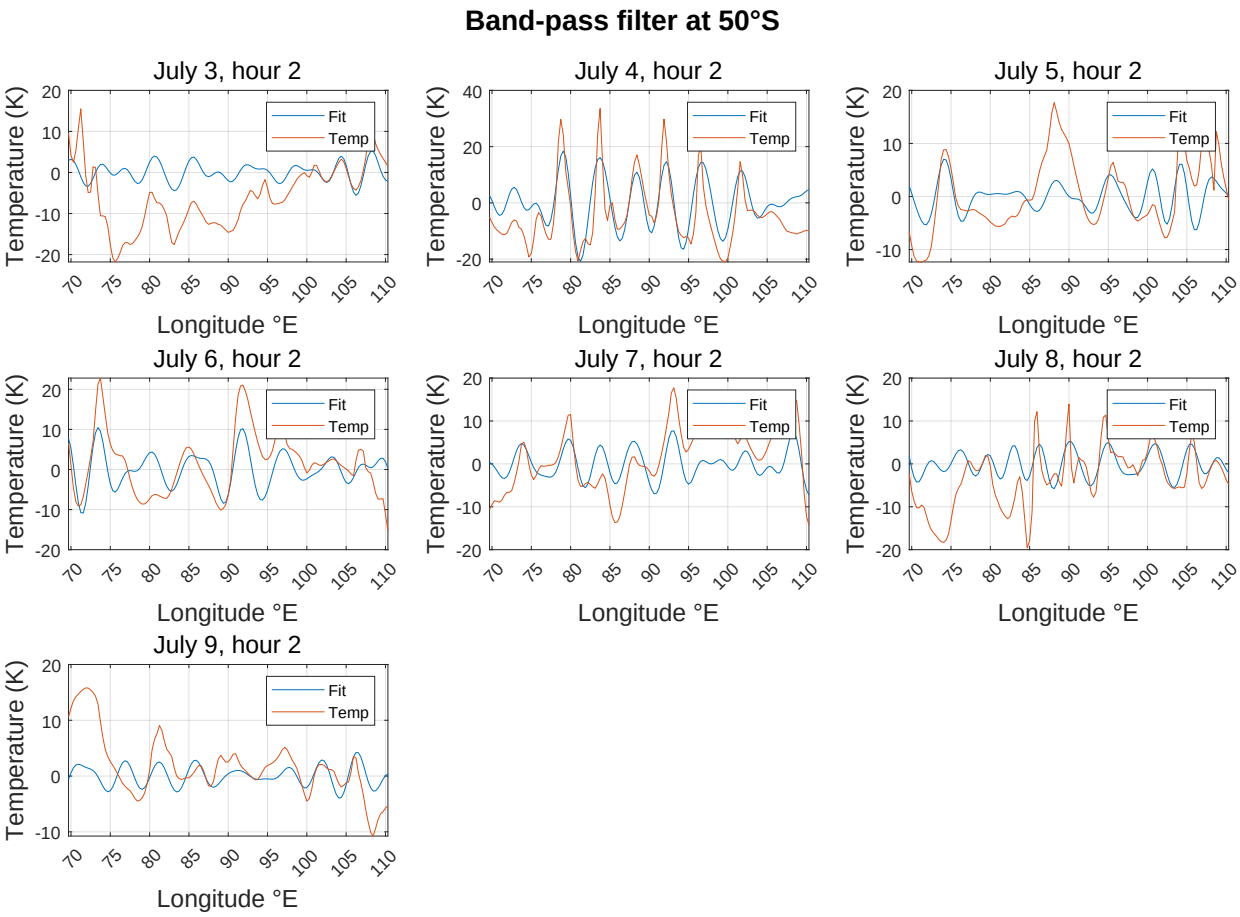

Figure 4.7: Band-pass filter used to isolated the desired GW. Filter designed in Matlab, and same filter used for all hours of the different days. Only hour 2 are plotted for each day.

To be able to see the daily change in amplitude of the PW, the mean temperature of the different days was found and plotted for all longitudes. Compared this activity with its respective propagation, figure 4.5. The deviations in temperature of the small structures were calculated to highlight how the amplitude of the GW acted daily. This was done for the region of interest. Compared the activity with the previously found propagation, figure 4.6.

The activity of PW in temperature over each of the seven different days is presented in figure 4.8. The contour plot is over all longitudes. There is a warm area from 0°E to -180°E relative to the area from 0°E to 180°E, with a gradient between the two sides. Each of the days has a different maximum and minimum temperature. Hence, there are some hot spots in the warm area and vice versa for the cold. Figure 4.9 is a contour plot of the activity of GW given the amplitude variations. The longitude range from 70°E to 110°E is plotted for the seven days. Each day has a different intensity in the fluctuations over the longitudes presented and seemingly no uniform pattern. Some include more spikes in activity than others, but not in any clear order by just looking at the figure.

Figures 4.8 and 4.9 are presented sideways on the next pages to display the plots with the most accuracy.

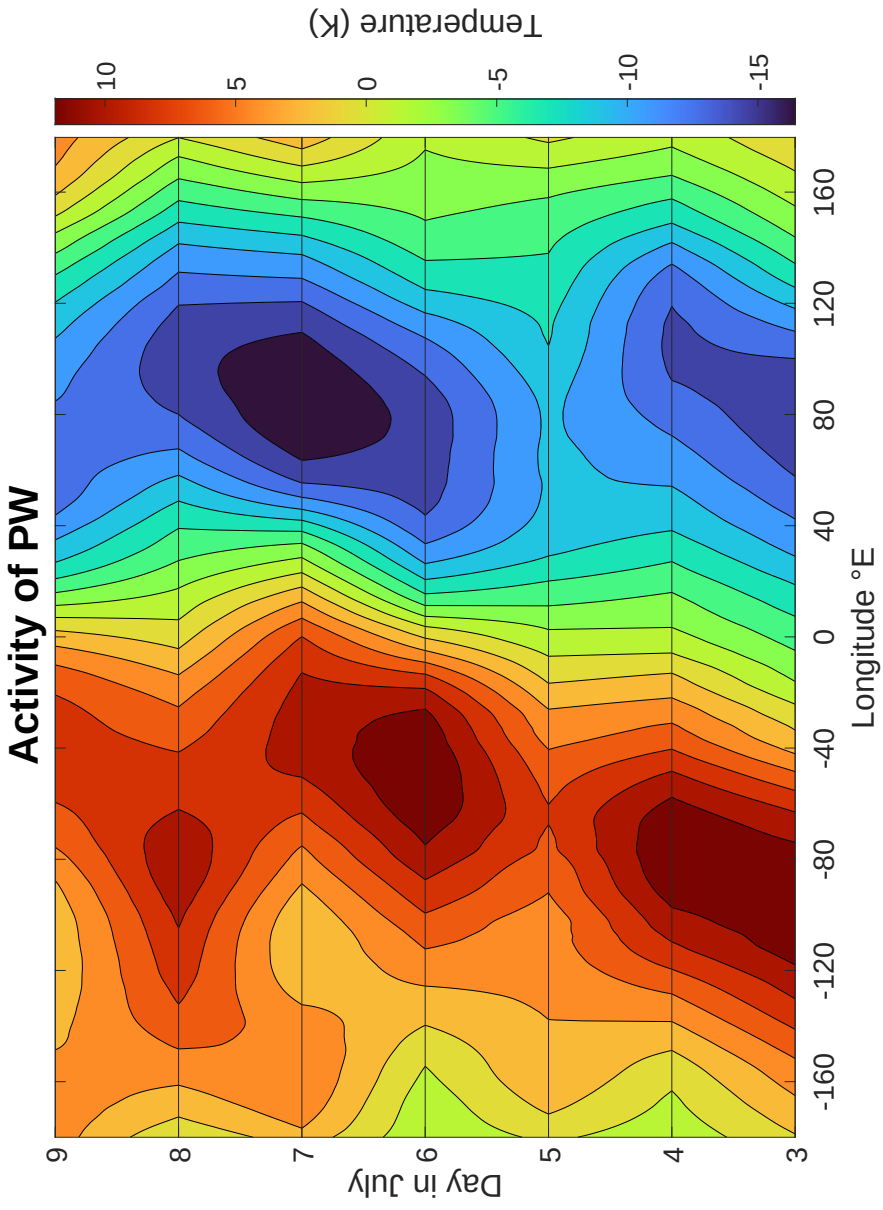

Figure 4.8: The activity of the PW given the temperature variations over the seven days for all longitudes at 50°S.

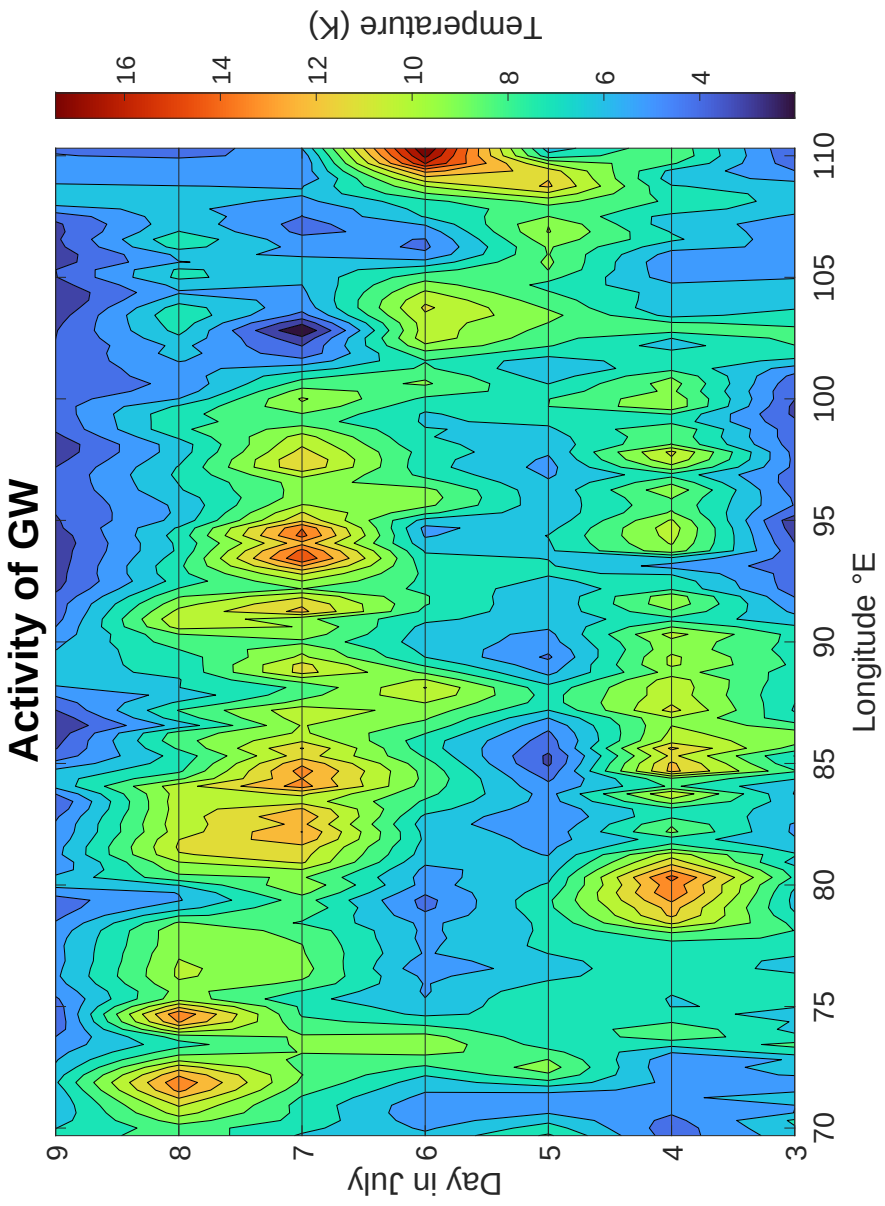

Figure 4.9: The activity of the GW given the temperature variations. The contour plots are displaying a specific range of longitudes.

Found the daily mean amplitude over the range of longitude in the region of interest. This was done for each day on both PW and GW, and both graphs were plotted. To calculate a linear correlation coefficient between the mentioned graphs, Matlab function corr [21] was utilized.

The daily mean temperature in the range 70°E to 110°E for both PW and GW is presented in figure 4.10. The plot contains two y-axes with different temperature scales. Both waves have an alternating tendency but have peaks on different days. The correlation of -0.54 between the waves is presented in a text box in the figure.

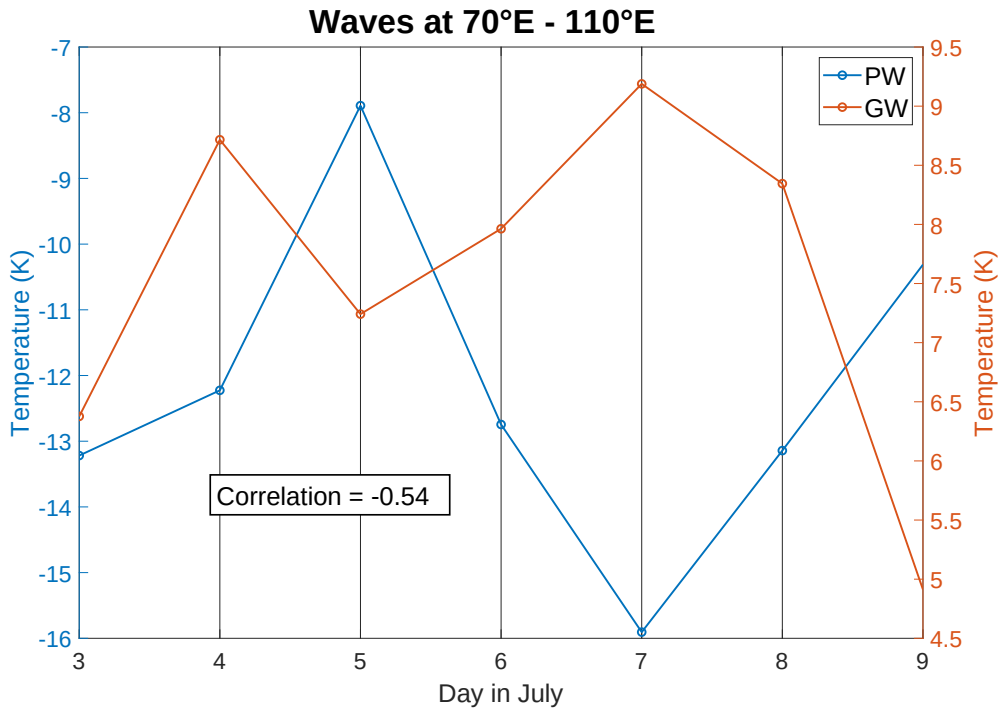

Figure 4.10: The daily mean temperatures of PW and GW over the chosen domain in the seven days of July. Also displays the correlation between the two graphs. Notice that there are two y-axes.

5 Discussion

This section will examine the results, what the key findings from the prelude [3] were, the propagation of the waves, and the found interaction. An interpretation of the wave interaction will be given and compared with findings in other papers. In addition, limitations in this study and propositions for future work.

5.1 Detected GW from prelude and chosen altitude

As stated in the project report, a promising wave packet of GW was found and traced at approx. 70 km, meaning in the middle of the mesosphere. Tracing the location down to the Earth's surface, the GW is just east of the Kerguelen Islands and Heard Island and McDonald Islands (see figure 5.1) in the Southern Ocean. These small islands are some of the most remote places on Earth [19], and due to no form of shielding, these islands are exposed to extreme wind conditions [33]. The Kerguelen Islands and Heard Island and McDonald Islands have peak altitudes of 1850 m and 2745 m, respectively. Thereby, the islands could be generating lee waves leading to the wave packet detected in the mid mesosphere, which was the main result of the project report.

The study by Alexander et al. [1] investigated what they refer to as "missing drag" in the southern hemisphere. 14 remote islands are examined in a period from May to September, including Kerguelen and Heard. Over both islands, similar results were obtained. The study identified wave patterns extending eastward by using temperature fluctuations, the same method used in the prelude to this thesis.

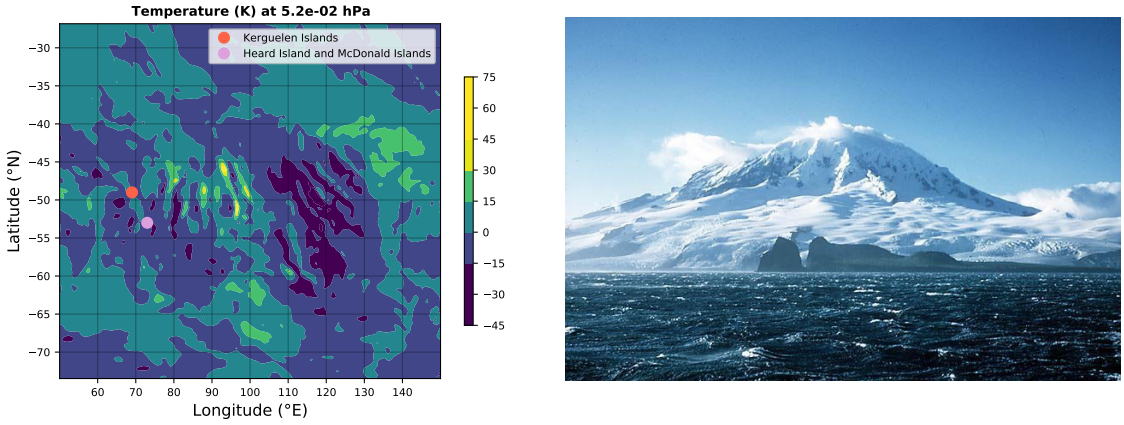

Figure 5.1: (a) The geographic location of the Kerguelen Islands and Heard Island and McDonald Islands in the region of interest. (b) Mawson Peak is, with an elevation of 2745 m, the highest peak at Heard Island (photo by [14], courtesy of Australian Antarctic Division)

The interactions between PW and GWs were examined at approx. 68 km above Earth's surface. This is the mid mesosphere, and figure 4.4 indicates that this is the point where the GWs amplitude reaches its peak. As far as studying interactions, this is ideal. The wave is close to or at its breaking point, making it highly sensitive to changes in the background winds. Given that the PW is a dominant perturbation in the net background wind, a change in the PW could make the GW break and dissipate its energy. If a lower altitude were to be examined, the change in PW would not be enough to reach the breaking point and a change in GW would be challenging to detect. As mentioned, after this altitude the amplitude gets more chaotic. There are some indications of a secondary GW being generated, but the vertical limitations make this difficult to state.

5.2 Propagation of the waves

Figure 4.5 shows how a zonal wave number 1 (S1) PW propagates during the period from July 3 to July 9. While it is a subtle eastward movement from day to day, it can be seen more clearly going vertical down from July 3 to July 6 to July 9 on the plot. A rough estimate gives that the PW has a velocity of 10° per day. This subtle move is to be expected, and was also found in the northern hemisphere by Stray et al. [35], where the wind was the parameter analyzed. It could be tempting to state this is a 36-day PW, but these plots only display the superposition of all S1. For the general interaction between GW and PW, the components of the superposition are not significant, the GW is only affected by the total. The region where the GW is found is in the trough of the wave displayed in the different plots.

The propagation of the GW is depicted in figure 4.6. Some of the days show promising propagation patterns, but two days stand out with clear temperature fluctuations. On July 4 a solid wave pattern can be seen in the first 6 hours of the day and appears again at some longitudes at about hour 16. The pattern on July 7 has more continuity, it goes from hour 3 to hour 17 and is located from 70°E - 100°E. Common for both of these days, the propagation is eastward with approx. the same velocity. The velocity can be estimated to be around 50 km/h when taken into account the latitude. The other days in July display some local wave propagation, but only small patches. The pattern in the background of all days should be ignored, they occur due to the filters that are used to highlight the small-scale GW. Taking into consideration that the contour plots are on the same color gradient, there could be more wave structures in several days, but in that case much weaker signals.

5.3 Amplitude and activity of the waves

In figures 4.8 and 4.9, the daily activity of the waves is plotted by their amplitude fluctuations. Starting with PW and figure 4.8, the same eastward propagation as in figure 4.5 can be detected. At the region of interest, 70°E - 100°E, the amplitude goes through two troughs/peaks over the course of the days. Starting at a low on July 3, to a peak on July 5, going down to a trough on July 7, and ending at a high on July 9. Meaning that the wind velocity follows a close to wave shape when seen as time-dependent.
The activity of GW is in line with the propagation in figure 4.6. From figure 4.9, there is clear that July 4 and July 7 contain the most fluctuations in amplitude, meaning more activity. This corresponds well with figure 4.6. The few peaks during the other days, like between 70°E - 75°E on July 8, can be recognized in their respective contour plots, but not as significant. The key finding in figure 4.9 is which days that have an occurrence of GW, and how dominant the fluctuations are. Analyzing the time dependency, there is a similarity with the activity of PW, two troughs/peaks.

To further examine this similarity or correlation, figure 4.10 displays both activities over the region of interest as a function of time. To an extent, both have a sinusoidal shape, just out of phase with each other. The correlation coefficient presented in the figure is -0.54, i.e. the two waves anti correlates. Considering the two graphs, the anti-correlation is quite clear. Only on July 3, there is an offset in the anti-correlation.

5.4 Interaction and interpretation

The PW and GW are found by temperature fluctuations around a mean temperature at a chosen altitude (~68 km) and latitude (50°S). This means temperature could vary due to seasonal variation, but given the period in this data being a few days, it can be considered constant. The primary effect on the GW propagation would be due to wind. If the data on the wind could be extracted and analyzed, a similar behavior would most likely be detected, fluctuations around a mean value around the globe.

The net wind speed the GW is propagating in can be simplified to the sum of seasonal mean wind and PW wind. The PW wind will in general depend on the longitude and its amplitude. Given that the longitudes of the region of interest are 70°E - 110°E, a relatively small range, the PW part will manly vary only in time. If the amplitude of the PW makes the net wind equal to or greater than the flow of GW, the GW pattern will not occur. At the point where the winds are equal, the GW will reach the critical level and break. As mentioned, and depicted in figure 4.4, the GW in this analysis is on the verge of the critical level. Figure 4.10 and the calculated coefficient verify this. The amplitude of the PW grows, leading to attenuation of the GW or perhaps even breaking, before the PW amplitude decreases and the GW can propagate once again. July 4 and July 7 stand out as the clearest result on this, the PW is low compared to GW and from figure 4.6 this is when the propagation occurs.

This physical interpretation of the interaction found can be explained through temperatures as well. By looking at the vertical temperature gradients generated by the seasonal mean, PW, and GW. At some times and longitudes, the PW will cause a steeper temperature gradient, making the net slope exceed the DALR. The argument is, in the end, the same, the amplitude of PW increases to the point where it contributes to the GW dissipating energy, breaking and stopping propagating.
Ramesh et al. [31] showed, in their study, that the mesospheric temperature inversion was mainly caused due to GW breaking and that the inversion amplitudes got modulated by the interaction between PWs and GWs. In a paper by Miyahara [28], it is stated that the amplitudes of PWs are reduced by the drag forces due to small-scale GWs breaking in the mesosphere. These papers correspond with the findings found. Considering figure 4.10, the GW breaking is not an instantaneous process. Meaning that GW could be breaking while the PW amplitude is high, leading to attenuation of the PW and the GW can retain its energy and attain large amplitude. This will then allow PW to grow once again, leading the GW to start breaking. If this is the case, the interaction found is effectively an oscillatory feedback mechanism.

The interaction may not be direct. In the atmosphere, there is all kind of waves and several of them are filtered out through the analysis. One is tides, which could be interacting with PW and GW, as an intermediate stage. In that scenario, the PW interaction with GW would be indirect. This is mentioned in the paper of Williams et al. [38], where the coupling of PWs, tides, and GWs in the MLT was analyzed through measurements from a meteor radar.
A quick analysis, by taking the deviation of the PW, of the tides indicated a strong correlation between tides and GW and conversely anti-correlation with PW. This is presented in figures A.1 and A.2 in the appendix. It is important to remember that a correlation does not automatically lead to causality, but that the interaction between PW and GW goes through the tides is an alternative explanation.
Alexander et al. [2] suggests that lee wave drag generated from remote islands, like the Kerguelen and Heard and McDonald, is needed in the parameterization in models. The findings in this study concur with that suggestion and indicate that the GW from island topography can have a significant impact at higher altitudes.

5.5 Limitations

- As mentioned in Liu et al. [22], to be able to get a full description of the atmosphere, from planetary winds to turbulence, a spatial grid of $\sim 10^{21}$ would be needed. This is not feasible for computers at the current date.
- A simple median filter is used to filter out the unwanted scales of waves in the data. To properly be able to isolate a specific wave, a more complex filtering method could be applied.
- Only one variable, temperature, was used to inspect the interactions between the two waves, a second confirmation would be in a good scientific manner. A horizontal wind velocity had been preferable to verify the findings.
- This analysis is done on a personal computer with limited computing resources, which could affect the running time of the codes used.

5.6 Future work

To analyze the wind velocity and see if the findings correspond would be an obvious path for future work. The WCCAM5 simulation in this thesis goes from July 1-10, so even though it may not make a significant difference, more data could be obtained. There is also the opportunity to analyze other months to see if there is any seasonal variation when considering interactions.
The plausible alternative with tides being an intermediate stage in the interaction between PW and GW could be explored further. Such as analyzing the interaction more on an hourly basis. Further-

more, specifying whether some tides are more dominant could be a possibility. The results of this thesis strongly argue that studies of this alternative are of interest.
To verify the findings by examining wave interaction over other geographical locations is an opportunity. By employing the same method in other areas, it could be argued whether these results are general or not. Given that the region of interest in this paper is over the southern hemisphere, a location over the northern hemisphere would be preferable. Not to dismiss other regions in the same hemisphere as of interest. As mentioned, the presentation by Alexander et al. [1] highlights several other remote islands that could lead to similar findings.

Current climate and weather prediction models parameterize GW effects on the atmosphere. One element of these parameterizations is that the wave deposits its energy and momentum vertically above its source region. In a model resolving waves and their propagation, one could assess whether non-vertical propagation has a significant effect in these models.
WACCM5 had an upper vertical limitation of approx. 145 km. An improved version called WACCM-X goes vertically up to include the Exosphere, approx. 700km in altitude [24]. This model enables further examination of wave behavior and interaction above the MLT. A GW resolving simulation up to about 700km would though be an expensive process, both in time and cost.

6 Conclusion

The main goal of this report was to investigate and analyze the interaction between PWs and GWs through a high-resolution model. A detection of GW was made by analyzing data from the model WACCM5. Findings indicate that remote islands in the south Indian Ocean were the source of generation. The wave propagated upwards to the MLT, where the interaction with a PW where examined. The PW found was a zonal wave number 1 and propagated slightly towards the east. The period available in the simulation data was from July 3 to July 9.

Calculating the correlation coefficient between the amplitudes of the GW and PW gave an anti-correlation of -0.54. Hence, the amplitude of a PW decreased as the GW increased, and vice versa. Whether the correlation found is the same as causation is difficult to interpret. The circulation in the atmosphere is complex, so further studies are needed to confirm this. Nevertheless, an interaction between PW and GW was detected, direct or indirect.
The interaction found indicates that remote islands with high mountain peaks indeed can cause a significant change as high as the MLT. Furthermore, this highlights the importance of implementing islands like these correctly to atmospheric models.

References

[1] M Joan Alexander et al. *Mountain Wave Momentum Fluxes in the Southern Hemisphere from Satellite Measurements*. en. 2011. URL: https://airs.jpl.nasa.gov/system/presentations/files/118_alexander-SHmountainwaves.pdf.

[2] M. Joan Alexander et al. "Momentum flux estimates for South Georgia Island mountain waves in the stratosphere observed via satellite". en. In: *Geophysical Research Letters* 36.12 (2009). _eprint: https://onlinelibrary.wiley.com/doi/pdf/10.1029/2009GL038587. ISSN: 1944-8007. DOI: 10.1029/2009GL038587. URL: https://onlinelibrary.wiley.com/doi/abs/10.1029/2009GL038587 (visited on 06/13/2022).

[3] Håvar Alexandersen. *Interaction of planetary and gravity waves in a high-resolution model*. English. Tech. rep. Trondheim, Dec. 2021. (Visited on 12/21/2021).

[4] David G Andrews. "Atmospheric thermodynamics". English. In: *An Introduction to Atmospheric Physics, Second Edition*. Second Edition. Cambridge University Press, Apr. 2010, pp. 19–47. ISBN: 978-0-511-72966-9.

[5] David G Andrews. "Further atmospheric fluid dynamics". English. In: *An Introduction to Atmospheric Physics, Second Edition*. Second Edition. Cambridge University Press, Apr. 2010, pp. 119–146. ISBN: 978-0-511-72966-9.

[6] David G Andrews. "Introduction". English. In: *An Introduction to Atmospheric Physics, Second Edition*. Second Edition. Cambridge University Press, Apr. 2010, pp. 1–18. ISBN: 978-0-511-72966-9.

[7] David G Andrews. "Some atmospheric observations". English. In: *An Introduction to Atmospheric Physics, Second Edition*. Second Edition. Cambridge University Press, Apr. 2010, pp. 7–16. ISBN: 978-0-511-72966-9.

[8] *CFTool*. URL: https://se.mathworks.com/help/curvefit/curvefitting-app.html (visited on 12/20/2021).

[9] P. J. Espy. *Our Friend the Gravity Wave*. en. Stockholm University, May 2016.

[10] P. J. Espy. *Wind and waves*. English. 2016.

[11] *filterDesigner*. URL: https://se.mathworks.com/help/dsp/ug/using-filter-designer.html (visited on 05/20/2022).

[12] David C. Fritts and M. Joan Alexander. "Gravity wave dynamics and effects in the middle atmosphere". en. In: *Reviews of Geophysics* 41.1 (Apr. 2003). ISSN: 87551209. DOI: 10.1029/2001RG000106. URL: http://doi.wiley.com/10.1029/2001RG000106 (visited on 12/19/2021).

[13] Marvin Geller et al. "A Comparison between Gravity Wave Momentum Fluxes in Observations and Climate Models". In: *Journal of Climate* 26 (Sept. 2013), pp. 6383–6405.

[14] A.J. Graff. *Big Ben, Heard Island*. 2010. URL: http://www.skimountaineer.com/ROF/OcAnt/BigBen/BigBenHeardIsland.jpg.

[15] Dennis L. Hartmann. *Global physical climatology*. en. International geophysics v. 56. San Diego: Academic Press, 1994. ISBN: 978-0-12-328530-0.

[16] W.K. Hocking. *Buoyancy (gravity) waves in the atmosphere*. English. 2001. URL: https://physics.uwo.ca/~whocking/p103/grav_wav.html (visited on 12/20/2021).

[17] James R. Holton. "The Influence of Gravity Wave Breaking on the General Circulation of the Middle Atmosphere". EN. In: *Journal of the Atmospheric Sciences* 40.10 (Oct. 1983). Publisher: American Meteorological Society Section: Journal of the Atmospheric Sciences, pp. 2497–2507. ISSN: 0022-4928, 1520-0469. DOI: 10.1175/1520-0469(1983)040<2497:TIOGWB>2.0.CO;2. URL: https://journals.ametsoc.org/view/journals/atsc/40/10/1520-0469_1983_040_2497_tiogwb_2_0_co_2.xml (visited on 12/19/2021).

[18] Ki-Hwan Kim et al. "A Simple Method to Find a Neighboring Grid Point on the Cubed-sphere". en. In: *Asia-Pacific Journal of Atmospheric Sciences* 54.S1 (June 2018), pp. 413–419. ISSN: 1976-7633, 1976-7951. DOI: 10.1007/s13143-018-0027-x. URL: http://link.springer.com/10.1007/s13143-018-0027-x (visited on 06/14/2022).

[19] Talia Lakritz. *The 20 most isolated places on Earth*. en-US. Jan. 2019. URL: https://www.insider.com/worlds-most-isolated-remote-places-2017-10 (visited on 06/23/2022).

[20] R. S. Lindzen. "Turbulence and stress owing to gravity wave and tidal breakdown". en. In: *Journal of Geophysical Research* 86.C10 (1981), p. 9707. ISSN: 0148-0227. DOI: 10.1029/JC086iC10p09707. URL: http://doi.wiley.com/10.1029/JC086iC10p09707 (visited on 12/19/2021).

[21] *Linear or rank correlation - MATLAB corr - MathWorks Nordic*. URL: https://se.mathworks.com/help/stats/corr.html (visited on 05/21/2022).

[22] H.-L. Liu et al. "Gravity waves simulated by high-resolution Whole Atmosphere Community Climate Model". en. In: *Geophysical Research Letters* 41.24 (Dec. 2014), pp. 9106–9112. ISSN: 00948276. DOI: 10.1002/2014GL062468. URL: http://doi.wiley.com/10.1002/2014GL062468 (visited on 12/19/2021).

[23] H.-L. Liu. "Large Wind Shears and Their Implications for Diffusion in Regions With Enhanced Static Stability: The Mesopause and the Tropopause". en. In: *Journal of Geophysical Research: Atmospheres* 122.18 (Sept. 2017), pp. 9579–9590. ISSN: 2169-897X, 2169-8996. DOI: 10.1002/2017JD026748. URL: https://onlinelibrary.wiley.com/doi/10.1002/2017JD026748 (visited on 12/19/2021).

[24] Han-Li Liu et al. "Development and Validation of the Whole Atmosphere Community Climate Model With Thermosphere and Ionosphere Extension (WACCM-X 2.0)". en. In: *Journal of Advances in Modeling Earth Systems* 10.2 (Feb. 2018), pp. 381–402. ISSN: 1942-2466, 1942-2466. DOI: 10.1002/2017MS001232. URL: https://onlinelibrary.wiley.com/doi/10.1002/2017MS001232 (visited on 06/16/2022).

[25] Liu, Hanli. *WACCM-SE NE120 F2000 July*. Type: dataset. 2020. DOI: 10.5065/RXAE-AB06. URL: https://dashrepo.ucar.edu/dataset/id/42f0cb12-5dfd-4950-97b6-91d749964620.html (visited on 12/20/2021).

[26] *Lomb-Scargle periodogram*. URL: https://se.mathworks.com/help/signal/ref/plomb.html (visited on 12/20/2021).

[27] *Median filter*. URL: https://docs.scipy.org/doc/scipy/reference/generated/scipy.ndimage.median_filter.html (visited on 12/20/2021).

[28] Saburo Miyahara. "Suppression of Stationary Planetary Waves by Internal Gravity Waves in the Mesosphere". en. In: *Journal of the Atmospheric Sciences* 42.1 (Jan. 1985), pp. 100–112. ISSN: 0022-4928, 1520-0469. DOI: 10.1175/1520-0469(1985)042<0100:SOSPWB>2.0.CO;2. URL: http://journals.ametsoc.org/doi/10.1175/1520-0469(1985)042%3C0100:SOSPWB%3E2.0.CO;2 (visited on 06/08/2022).

[29] National oceanic and atmospheric administration, National aeronautics and space administration, and United States Air Force. *U.S. STANDARD ATMOSPHERE, 1976*. English. Oct. 1976. URL: https://www.ngdc.noaa.gov/stp/space-weather/online-publications/miscellaneous/us-standard-atmosphere-1976/us-standard-atmosphere_st76-1562_noaa.pdf (visited on 12/20/2021).

[30] Manja Placke et al. "Testing linear gravity wave theory with simultaneous wind and temperature data from the mesosphere". en. In: *Journal of Atmospheric and Solar-Terrestrial Physics* 93 (Feb. 2013), pp. 57–69. ISSN: 13646826. DOI: 10.1016/j.jastp.2012.11.012. URL: https://linkinghub.elsevier.com/retrieve/pii/S1364682612002854 (visited on 12/19/2021).

[31] Dr. K. Ramesh et al. "Planetary wave-gravity wave interactions during mesospheric inversion layer events". In: *Journal of Geophysical Research* 118 (July 2013), pp. 1–13. DOI: 10.1002/jgra.50379.

[32] Murry L. Salby. “Atmospheric Waves”. en. In: *Fundamentals of atmospheric physics*. International geophysics series v. 61. San Diego: Academic Press, 1996, pp. 426–487.

[33] Iain Staffell and Stefan Pfenninger. “Using bias-corrected reanalysis to simulate current and future wind power output”. en. In: *Energy* 114 (Nov. 2016), pp. 1224–1239. ISSN: 0360-5442. DOI: 10.1016/j.energy.2016.08.068. URL: https://www.sciencedirect.com/science/article/pii/S0360544216311811 (visited on 12/20/2021).

[34] Nora Stray et al. “Observations of PW activity in the MLT during SSW events using a chain of SuperDARN radars and SD-WACCM”. In: *Atmospheric Chemistry and Physics Discussions* 15 (Jan. 2015), pp. 393–413. DOI: 10.5194/acpd-15-393-2015.

[35] Nora H. Stray et al. “Characterisation of quasi-stationary planetary waves in the Northern MLT during summer”. en. In: *Journal of Atmospheric and Solar-Terrestrial Physics* 127 (May 2015), pp. 30–36. ISSN: 13646826. DOI: 10.1016/j.jastp.2014.12.003. URL: https://linkinghub.elsevier.com/retrieve/pii/S1364682614002855 (visited on 06/08/2022).

[36] *Unidata | NetCDF*. 2021. URL: https://www.unidata.ucar.edu/software/netcdf/ (visited on 12/21/2021).

[37] John M. Wallace and Peter Victor Hobbs. “Introduction and Overview”. en. In: *Atmospheric science: an introductory survey*. 2nd ed. International geophysics series v. 92. OCLC: ocm62421169. Amsterdam ; Boston: Elsevier Academic Press, 2006, pp. 1–22. ISBN: 978-0-12-732951-2.

[38] P.J.S. Williams et al. “The coupling of planetary waves, tides and gravity waves in the mesosphere and lower thermosphere”. en. In: *Advances in Space Research* 24.11 (Jan. 1999), pp. 1571–1576. ISSN: 02731177. DOI: 10.1016/S0273-1177(99)00881-9. URL: https://linkinghub.elsevier.com/retrieve/pii/S0273117799008819 (visited on 05/23/2022).

[39] Corwin J. Wright et al. “Exploring gravity wave characteristics in 3-D using a novel S-transform technique: AIRS/Aqua measurements over the Southern Andes and Drake Passage”. en. In: *Atmospheric Chemistry and Physics* 17.13 (July 2017), pp. 8553–8575. ISSN: 1680-7324. DOI: 10.5194/acp-17-8553-2017. URL: https://acp.copernicus.org/articles/17/8553/2017/ (visited on 06/24/2022).

Appendix

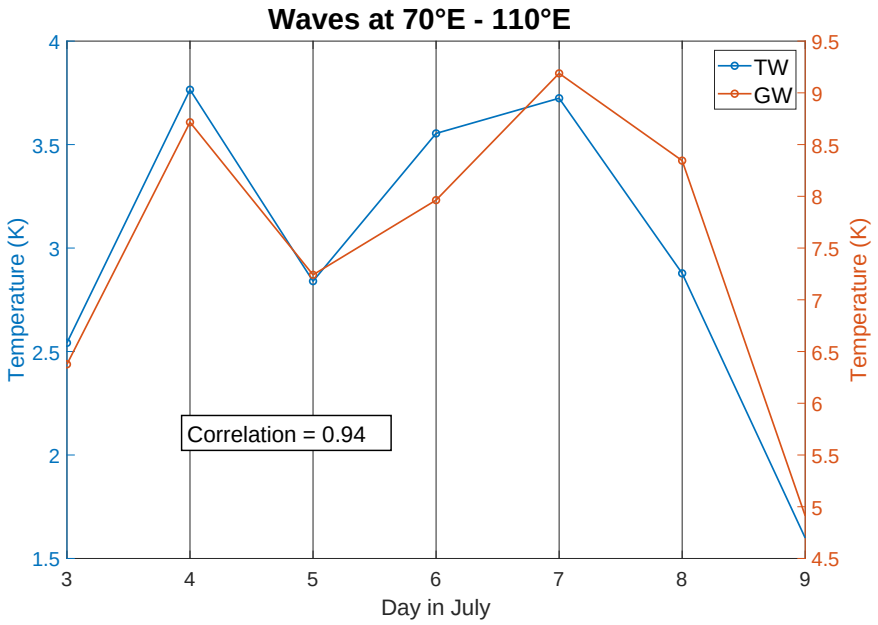

Figure A.1: The daily mean temperatures of tides (TW) and GW over the chosen domain in the seven days of July. Also displays the correlation between the two graphs. Notice that there are two y-axes. Tides were found by taking the deviation of the PW.

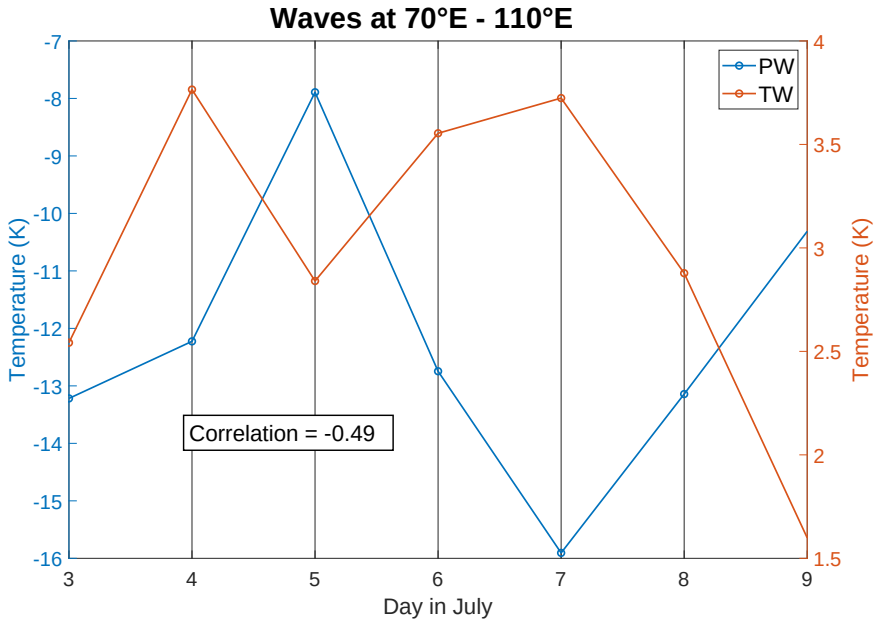

Figure A.2: The daily mean temperatures of PW and tides (TW) over the chosen domain in the seven days of July. Also displays the correlation between the two graphs. Notice that there are two y-axes. Tides were found by taking the deviation of the PW.

Table 2: All the coordinates (coord) and variables (var) of the data set from the WACCM5 simulation. Each variable has a total amount of values given by the dimensions of its coordinates. The table represents one day. Each day had the same structure in coordinates and variables.

Name	Type	Long name	Dependence	Dimensions	Units
lev	coord	Hybrid level at midpoints	-	209	hPa
ilev	coord	Hybrid level at interfaces	-	210	hPa
time	coord	Time	-	24	hours
lat	coord	Latitude	-	768	degrees north
lon	coord	Longitude	-	1152	degrees east
hyam	var	Hybrid A coefficient at layer midpoints	lev	-	-
hybm	var	Hybrid B coefficient at layer midpoints	lev	-	-
P0	var	Reference pressure	-	-	Pa
hyai	var	Hybrid A coefficient at layer interfaces	ilev	-	-
hybi	var	Hybrid B coefficient at layer interfaces	ilev	-	-
OMEGA	var	Vertical velocity	time,lev,lat,lon	-	Pa/s
PS	var	Surface pressure	time,lat,lon	-	Pa
T	var	Temperature	time,lev,lat,lon	-	K
Z3	var	Geopotential height	time,lat,lon	-	m

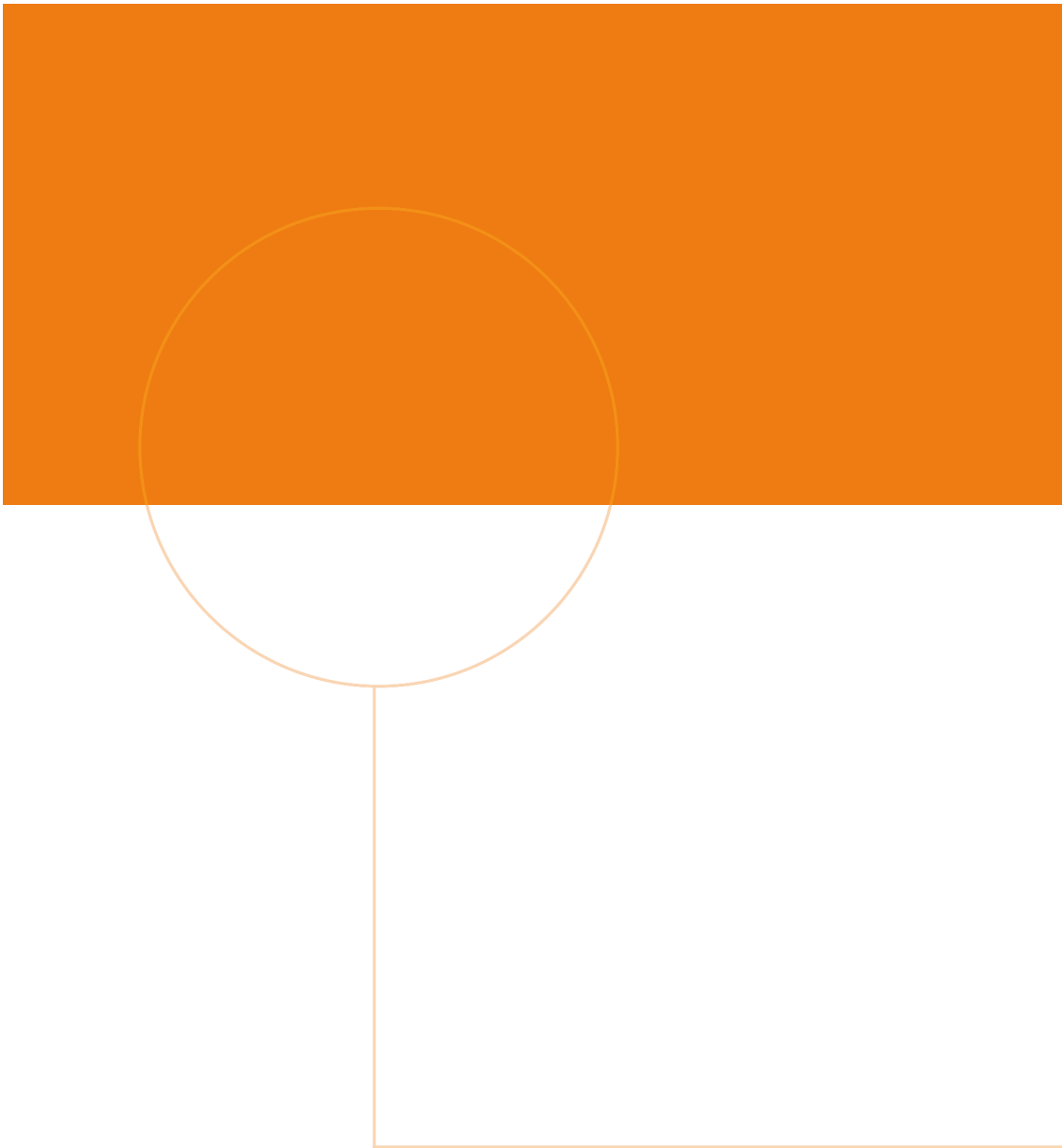

NTNU

Norwegian University of
Science and Technology